The Astrophysical Journal, 873:116 (19pp), 2019 March 10 https://doi.org/10.3847/1538-4357/ab05c8

Origin of a Massive Hyper-runaway Subgiant Star LAMOST-HVS1: Implication from *Gaia* and Follow-up Spectroscopy

Kohei Hattori[1], Monica Valluri[1], Norberto Castro[1,2], Ian U. Roederer[1,3], Guillaume Mahler[1], and Gourav Khullar[4,5]
[1] Department of Astronomy, University of Michigan, 1085 S. University Avenue, Ann Arbor, MI 48109, USA; khattori@umich.edu
[2] Leibniz-Institut für Astrophysik Potsdam (AIP), An der Sternwarte 16, 14482, Potsdam, Germany
[3] Joint Institute for Nuclear Astrophysics—Center for the Evolution of the Elements (JINA-CEE), USA
[4] Department of Astronomy and Astrophysics, University of Chicago, 5640 South Ellis Avenue, Chicago, IL 60637, USA
[5] Kavli Institute of Cosmological Physics, University of Chicago, 5640 South Ellis Avenue, Chicago, IL 60637, USA
Received 2018 October 3; revised 2019 February 6; accepted 2019 February 8; published 2019 March 12

Abstract

We report that LAMOST-HVS1 is a massive hyper-runaway subgiant star with a mass of 8.3 $M_\odot$ and super-solar metallicity, which was ejected from the inner stellar disk of the Milky Way ∼33 Myr ago with the intrinsic ejection velocity of 568^{+19}_{-17} km s^{-1} (corrected for the streaming motion of the disk), based on the proper motion data from *Gaia* Data Release 2 (DR2) and high-resolution spectroscopy. The extremely large ejection velocity indicates that this star was not ejected by the supernova explosion of a binary companion. Rather, it was probably ejected by a three- or four-body dynamical interaction with more massive objects in a high-density environment. Such a high-density environment may be attained at the core region of a young massive cluster (YMC) with mass of $\gtrsim 10^4\,M_\odot$. The ejection agent that took part in the ejection of LAMOST-HVS1 may be an intermediate mass black hole ($\gtrsim 100\,M_\odot$), a very massive star ($\gtrsim 100\,M_\odot$), or multiple ordinary massive stars ($\gtrsim 30\,M_\odot$). Based on the flight time and the ejection location of LAMOST-HVS1, we argue that its ejection agent or its natal star cluster is currently located near the Norma spiral arm. The natal star cluster of LAMOST-HVS1 may be an undiscovered YMC near the Norma spiral arm.

Key words: Galaxy: disk – Galaxy: kinematics and dynamics – open clusters and associations: general – stars: abundances – stars: early-type – stars: individual (LAMOST-HVS1)

1. Introduction

Young O- and B-type stars with large peculiar velocities ($\gtrsim$40 km s^{-1}) or with large vertical excursion from the Galactic disk plane ($\gtrsim$1 kpc) are called runaway stars. Some runaway stars are massive ($\gtrsim 8\,M_\odot$; O-type and early B-type), and are thought to have been ejected from their birth places in the stellar disk. The recently published astrometric data from *Gaia* (Gaia Collaboration et al. 2018) have given us a unique opportunity to accurately reconstruct the orbits of these short-lived massive runaway stars and to measure their ejection locations and velocities. This analysis enables us not only to investigate the processes by which such runaway stars are ejected but also provide new insights into the environments where massive stars form.

The proposed mechanisms for ejecting massive runaway stars may be categorized into two classes (Blaauw 1993):

1. Binary ejection mechanism (BEM), in which a runaway star is ejected as a result of the supernova explosion of its binary companion (Zwicky 1957; Blaauw 1961); and
2. Dynamical ejection mechanism (DEM), in which three- or four-body interaction of stars (and black holes) in high-density environment ejects a runaway star (Poveda et al. 1967; Aarseth & Hills 1972; Hut & Bahcall 1983).

In this work, we adopt the above nomenclature and acronyms BEM and DEM from Silva & Napiwotzki (2011).

The most striking difference between these two mechanisms is the range of intrinsic ejection velocity $V_{\rm ej}^{\rm int}$ of runaway stars with respect to the original binary system (in the case of BEM) or the natal star cluster (in the case of DEM).

In the BEM, the ejection velocity is determined by the orbital velocity at the time of the supernova explosion and the kick velocity arising from the asymmetry of the supernova. Tauris (2015) showed that BEM ejects massive runaway stars of $M = 10\,M_\odot$ with a velocity up to $V_{\rm ej}^{\rm int} = 320$ km s^{-1}. By taking into account the fact that less massive stars can be ejected with larger velocity (Portegies Zwart 2000), we estimate that a B-type main-sequence star with $8\,M_\odot$—such as LAMOST-HVS1, which is the subject of this paper—may be ejected with a velocity up to $V_{\rm ej}^{\rm int} \sim 400$ km s^{-1} ($=320\,{\rm km\,s^{-1}} \times 10\,M_\odot/8\,M_\odot$), by this mechanism.

For DEM, the ejection velocity is determined by the details of how the binary system is disrupted by the third (and fourth) object and the ejection velocity is always smaller than the surface escape velocity from the most massive object involved in the few-body interaction (Leonard 1991). The surface escape velocity from an object with mass M_* and radius R_* is given by[6]

$$v_{{\rm esc},*} = 618\ {\rm km\ s^{-1}} \sqrt{\frac{M_*}{M_\odot}\frac{R_\odot}{R_*}}\,, \tag{1}$$

where ($M_\odot$, $R_\odot$) are the mass and radius of the Sun. As is obvious from this expression, this can be enormous for very massive compact objects. As a result, the ejection velocity of a massive runaway star with $M \simeq 8\,M_\odot$ can, in principle, reach $V_{\rm ej}^{\rm int} \sim 10^3$ km s^{-1} if a compact object such as a very massive star (VMS) (Gvaramadze et al. 2009) participates in the

[6] In this paper, both the stellar radius and the Galactocentric radius in the cylindrical coordinate system are expressed by R. However, the distinction between these quantities is obvious from the context.

few-body encounter. If a black hole participates in the few-body interaction, then the above argument is no longer valid (the surface escape velocity corresponds to the speed of light). However, simulations show that the typical ejection velocity can be as high as $\sim 10^3\,\mathrm{km\,s^{-1}}$ if an intermediate mass black hole (IMBH) participates in the few-body interaction (Gvaramadze et al. 2008; Fragione & Gualandris 2018; see also Hills 1988; Yu & Tremaine 2003).

For both BEM and DEM, theoretical studies suggest that a large ejection velocity of a runaway star is attained when some extreme conditions are met, such as very small separation of stars in a binary to be disrupted or the existence of a massive compact object (Tauris & Takens 1998; Gvaramadze et al. 2008, 2009). Thus, massive runaway stars in the Milky Way with large ejection velocity may provide some insights into the extreme environment in which massive stars form (Gies & Bolton 1986; Conlon et al. 1990; Hoogerwerf et al. 2001; de Wit et al. 2005; Mdzinarishvili & Chargeishvili 2005; Martin 2006; Silva & Napiwotzki 2011; Tetzlaff et al. 2011; Boubert et al. 2017; Maíz Apellániz et al. 2018).

In this regard, the recently discovered LAMOST-HVS1, a luminous blue star in the inner halo with an extremely large velocity (Zheng et al. 2014; Huang et al. 2017), is an intriguing object with which to study the extreme conditions of the ejection of runaway stars. As we will describe briefly in Section 2.1, proper motion information for this star from *Gaia* Data Release 2 (DR2; Gaia Collaboration et al. 2018), as well as its young age suggests that this star was not ejected by the supermassive black hole (SMBH) at the Galactic Center (as has been proposed for other hypervelocity stars) but was ejected from the stellar disk. Due to its (almost) unbound orbital energy, this star can be categorized as a massive hyper-runaway star. Based on its current velocity, its intrinsic ejection velocity is also expected to be quite large. This makes LAMOST-HVS1 a unique star with which we can recover important information about the extreme environments that result in massive star ejection.

In this paper, we investigate the origin of this massive hyper-runaway star LAMOST-HVS1 by analyzing its orbit and stellar atmosphere based on data from *Gaia* and our spectroscopic observation with *Magellan* Telescope. The outline of this paper is as follows. In Section 2, we describe the astrometric data from *Gaia* and argue that LAMOST-HVS1 was ejected from the Galactic disk. In Section 3, we derive the stellar parameters from our spectroscopic data and show that this star is unambiguously massive. In Section 4, we analyze the orbit of this star. In Section 5, we show the results of our analysis. In Section 6, we discuss the possible ejection mechanism of LAMOST-HVS1. In Section 7, we discuss the ejection rate for each possible ejection mechanism. Section 8 summarizes our conclusions.

2. Astrometric Data from *Gaia*-DR2

The astrometric data for LAMOST-HVS1 provided by *Gaia* DR2 (Gaia Collaboration et al. 2018) are summarized in Table 1. Here, we briefly describe these data and the simple conclusions that can be drawn from them. The proper motion of this star is precisely measured but the line-of-sight velocity of this star is not measured by *Gaia*. The *Gaia*-DR2 parallax is negative and is associated with a large error, and therefore we do not use this parallax information in our analysis. For the distance and the heliocentric line-of-sight velocity we use our spectroscopic data as discussed in Section 3. The reliability of the astrometric solution for this star is discussed in the Appendix.

Table 1
Basic Properties of LAMOST-HVS1

Gaia Data	LAMOST-HVS1
Gaia DR2 source_id	590511484409775360
ℓ	221.°099505130
b	35.°407214626
α	138.°027167145
δ	9.°272744019
G/mag	13.06
$(G_{\rm BP} - G_{\rm RP})$/mag	−0.2316
ϖ/mas	−0.044
σ_ϖ/mas	0.067
$\mu_{\alpha*}$/(mas yr^{-1})	−3.54
$\sigma_{\mu,\alpha*}$/(mas yr^{-1})	0.11
μ_δ/(mas yr^{-1})	−0.62
$\sigma_{\mu,\ \delta}$/(mas yr^{-1})	0.09
Spectroscopic Data	
$T_{\rm eff}$	18100 ± 400 K
$\log(g)$	3.42 ± 0.065
$v_{\rm los}$	615 ± 5 km s^{-1}
$v \sin(i)$	130 ± 20 km s^{-1}
$v_{\rm macro}$	164 ± 30 km s^{-1}
$v_{\rm micro}$	6 ± 1 km s^{-1}
age τ	$37.4^{+4.0}_{-3.7}$ Myr
(Current mass) M_*	$8.3^{+0.5}_{-0.4}\ M_\odot$
(Current radius) R_*	$9.3^{+1.0}_{-0.9}\ R_\odot$
DM	$16.40^{+0.52}_{-0.48}$
$d_{\rm spec}$	$19.1^{+5.1}_{-3.8}$ kpc
Result of Orbital Analysis	
d	$13.3^{+1.7}_{-1.5}$ kpc

Note. The posterior distribution of the distance after the orbital analysis is denoted as d, while the spectroscopic distance used as an input of the orbital analysis is denoted as $d_{\rm spec}$ (see Figure 4).

2.1. *LAMOST-HVS1 is a Hyper-runaway Star*

Stars that have been ejected by the SMBH at the Galactic Center are often called "hypervelocity stars" (Hills 1988; Yu & Tremaine 2003; Brown 2015). Due to the large line-of-sight velocity of LAMOST-HVS1, it has been thought that this star, which is marginally bound to the Milky Way, may be a hypervelocity star.

Hattori et al. (2018b) showed that for a star at the distance of LAMOST-HVS1 ($d \sim 10$–20 kpc), the azimuthal angular momentum L_z has to be extremely close to zero if it is ejected by the SMBH (since the potential of the Milky Way in this region is close to axisymmetric). They showed that if LAMOST-HVS1 was ejected from the Galactic Center, then its proper motion would have to lie in a very narrow range of values (see Figure 4(a) of Hattori et al. 2018b). However, *Gaia*'s high-precision proper motion measurements $(\mu_{\alpha*}, \mu_\delta) = (-3.54 \pm 0.11, -0.62 \pm 0.09)\,\mathrm{mas\,yr^{-1}}$ of LAMOST-HVS1 indicate that its observed proper motions are so different from those predicted in the Galactic-Center-origin scenario that these data alone rule out this mechanism.

Table 2
Chemical Abundances of LAMOST-HVS1

X	LAMOST-HVS1		B stars		Sun
	[X/H][a]	A(X)	$\langle A_{\rm B}^{3\ {\rm kpc}}({\rm X})\rangle$	$\langle A_{\rm B}^{8\ {\rm kpc}}({\rm X})\rangle$	$A_{\odot}$(X)
Si	0.60 ± 0.06	$8.11^{+0.05}_{-0.05}$	7.73 ± 0.05	7.50 ± 0.05	7.51 ± 0.03
Mg	0.33 ± 0.10	$7.93^{+0.06}_{-0.12}$	7.76 ± 0.05	7.56 ± 0.05	7.60 ± 0.04
C	0.26 ± 0.07	$8.69^{+0.05}_{-0.06}$	8.85 ± 0.10	8.33 ± 0.04	8.43 ± 0.05
N	0.35 ± 0.07	$8.18^{+0.05}_{-0.05}$	8.22 ± 0.11	7.79 ± 0.04	7.83 ± 0.05
O	0.17 ± 0.07	$8.86^{+0.05}_{-0.05}$	8.94 ± 0.05	8.76 ± 0.05	8.69 ± 0.05

Notes. A(X) denotes the abundance of LAMOST-HVS1 derived from our analysis. $\langle A_{\rm B}^{3\ {\rm kpc}}({\rm X})\rangle$ and $\langle A_{\rm B}^{8\ {\rm kpc}}({\rm X})\rangle$ denote the mean abundance of the B stars located at $R = 3$ kpc and 8 kpc, respectively, derived from Table 9 of Nieva & Przybilla (2012) and the literature values of the radial abundance gradient therein. $A_{\odot}$(X) denotes the abundance of the Sun taken from Asplund et al. (2009).
[a] Note that $[{\rm X/H}] = A({\rm X}) - A_{\odot}({\rm X})$ depends not only on A(X) but also on an external quantity $A_{\odot}$(X). Thus, any systematic error on $A_{\odot}$(X) can affect [X/H].

Furthermore, the young age of this star, which has already been inferred from LAMOST spectra (Zheng et al. 2014; Hattori et al. 2018b), combined with the above-mentioned simple analysis of the proper motion, suggests that LAMOST-HVS1 was born in the Galactic disk and was ejected to reach its current location several kpc away from the disk plane. Given its large current velocity, this star is almost unbound to the Milky Way and thus LAMOST-HVS1 is a hyper-runaway star.

3. Spectroscopic Data

3.1. Observation of LAMOST-HVS1

We observed LAMOST-HVS1 on 2018 January 12 using the *Magellan* Inamori Kyocera Echelle (MIKE) spectrograph (Bernstein et al. 2003) mounted on the 6.5 m Landon Clay Telescope (Magellan II) at Las Campanas Observatory, Chile. The $1\farcs0 \times 5\farcs0$ entrance slit and 2×2 detector binning yielded spectral resolving powers of $R \equiv \lambda/\Delta\lambda \sim 30{,}000$ and 25,500 on the blue and red spectrographs, respectively. Light entering the two spectrographs is split by a dichroic at $\approx$4950 Å. Observations were split into seven sub-exposures, and the total integration time was 1.7 hr. The spectra cover $3350\ {\rm Å} \leqslant \lambda \leqslant 9400\ {\rm Å}$, although the spectra redward of $\approx$8300 Å suffer from fringing. The spectra were reduced using the CarPy MIKE pipeline (Kelson et al. 2000; Kelson 2003), including overscan subtraction, flat field division, image co-addition, cosmic ray removal, sky and scattered light subtraction, rectification of the tilted slit profiles, spectrum extraction, and wavelength calibration based on ThAr comparison lamp spectra taken between science exposures. Final signal-to-noise ratios per pixel range from $\approx$50 at 3500 Å, $\approx$200 at 4500 Å, $\approx$140 at 5500 Å, to $\approx$150 at 6500 Å. These spectra can be distributed upon request.

3.2. Analysis of Spectra of LAMOST-HVS1

The stellar atmosphere analysis is based on a grid of synthetic atmosphere models built using the atmosphere/line formation code FASTWIND (Santolaya-Rey et al. 1997; Puls et al. 2005; Rivero González et al. 2012). The projected rotational ($\upsilon \sin i$) and macroturbulence velocities are estimated using the IACOB-BROAD code (Simón-Díaz & Herrero 2007, 2014).

The modeling of the data is carried out in two steps. Initially, the observed LAMOST-HVS1 spectrum is compared with the synthetic FASTWIND grid, retrieving the set of stellar parameters that best reproduce the main absorption lines in the data. The errors in the macroturbulence and rotational velocities are estimated using the Fourier approach and goodness-of-fit algorithms described in Simón-Díaz & Herrero (2007, 2014). Based on the best model, a new grid is designed exploring different chemical compositions using fine steps of 0.1 dex in the abundances of the elements displayed in the observations (i.e., Si, Mg, C, N and O) and, microturbulence in steps of $1\ {\rm km\ s^{-1}}$. In addition, two abundance values for helium, namely $Y = {\rm He/H} = 0.10$ (approximate solar abundance) and 0.15 (super-solar abundance), are tried; and we fix it to the solar abundance because it results in a better fit to the data. The observed spectrum is cross-matched with this new grid until we find the composition and microturbulence that are able to reproduce the different spectral features. A detailed description of the technique and main transitions used in the analysis can be found in Castro et al. (2012) (see also Lefever et al. 2010). The stellar parameters and chemical composition (and their 1σ random error) obtained from the quantitative analysis are listed in Tables 1 and 2. The best-fit synthetic spectrum and the observed spectrum are shown in Figure 1.

It is worth mentioning that we obtain a large macroturbulence from our analysis. Simón-Díaz et al. (2017) also found stars with large macroturbulence at similar mass ranges. Our estimation is indeed higher than their findings in the IACOB sample. Below $15\ M_{\odot}$, the authors suggest different mechanisms that could induce this additional broadening, including the presence of stellar spots, surface inhomogeneities, and stellar oscillations (Aerts et al. 2014).

The heliocentric line-of-sight velocity of LAMOST-HVS1 derived from our spectroscopy is $v_{\rm los} = 615 \pm 5\ {\rm km\ s^{-1}}$, which is consistent with the previous measurements by LAMOST, $611.65 \pm 4.63\ {\rm km\ s^{-1}}$ (Huang et al. 2017). This agreement probably suggests that this star is not in a binary system.

The stellar distance is estimated in the following manner. First, we draw 1000 samples of ($T_{\rm eff}$, $\log g$) from the error distribution mentioned above. Then, for each realization of ($T_{\rm eff}$, $\log g$), we make a point-estimate of the stellar radius R_* based on the rotating evolutionary tracks published by Ekström et al. (2012). For each set of ($T_{\rm eff}$, $\log g$, R_*) and the corresponding synthetic FASTWIND spectral energy distribution, we calculate the probability distribution function (PDF) of the distance given the observed optical and IR photometry of LAMOST-HVS1 (B and V from APASS DR9 Henden et al. 2016; J, H, K_s from

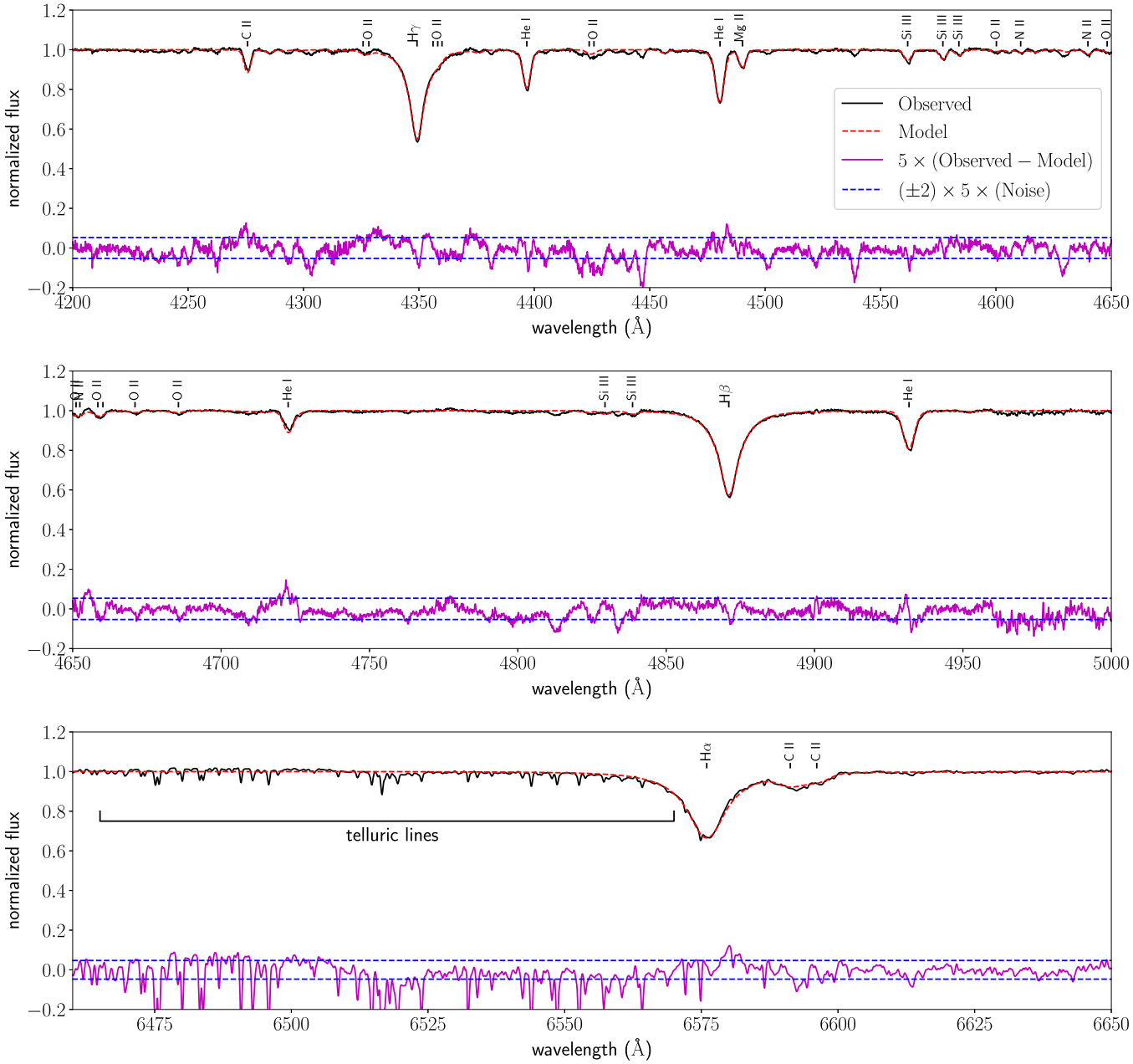

Figure 1. The normalized MIKE spectrum of LAMOST-HVS1 (black solid line) with some absorption lines annotated. The red-dashed line is the synthetic FASTWIND model using the best-fit parameters in Tables 1 and 2. We note that the helium abundance is fixed to approximate solar abundance. The residual spectrum (enlarged by a factor of five) is shown by the magenta solid line, and the 2σ noise level (enlarged by a factor of five) is shown by the blue-dashed lines. The high signal-to-noise ratio of our spectroscopic data and the good match with the model demonstrate the reliability of our stellar parameters and abundances. We note that the observed spectrum has not been shifted to the rest-frame. (That is, we do not correct the observed spectrum for the heliocentric line-of-sight velocity, $v_{\rm los} = 615$ km s^{-1}, and the observer's motion relative to the Sun, -13 km s^{-1}; we shift our model spectrum instead.) Analyzed metallic absorption lines are shown (by vertical line segment) only when the equivalent width is larger than 0.025 Å. Some absorption lines that are shown (by vertical line segment) but not annotated (e.g., those on both sides of Hγ line) are O_{II} lines. The sharp absorption features left to Hα are telluric lines.

2MASS Cutri et al. 2003; all of these quantities are listed in Table 1 in Hattori et al. 2018b). We adopt the standard Cardelli et al. (1989) extinction law with $R_V = 3.1$. The adopted color excess is $E(B-V) = 0.085$ for this star. Finally, we add these 1000 PDFs to obtain the full PDF of the spectroscopic distance $d_{\rm spec}$. *Gaia* reports a negative parallax ϖ for LAMOST-HVS1, but the median value of our spectroscopic distance is consistent with *Gaia*'s measurement within two standard deviations level ($|\varpi - 1/d_{\rm spec,median}| < 2\sigma_{\varpi}$).

3.3. Is LAMOST-HVS1 a Massive Star?

In general, heavier runaway stars are more difficult to accelerate to large velocities because they need to receive larger momentum (Portegies Zwart 2000). Thus, when studying the ejection mechanisms for a runaway star, it is important to accurately determine its stellar type (and hence its mass) (Silva & Napiwotzki 2011; McEvoy et al. 2017).

Our analysis suggests that LAMOST-HVS1 is a massive subgiant star with $M_* \simeq 8\,M_\odot$. To validate our stellar

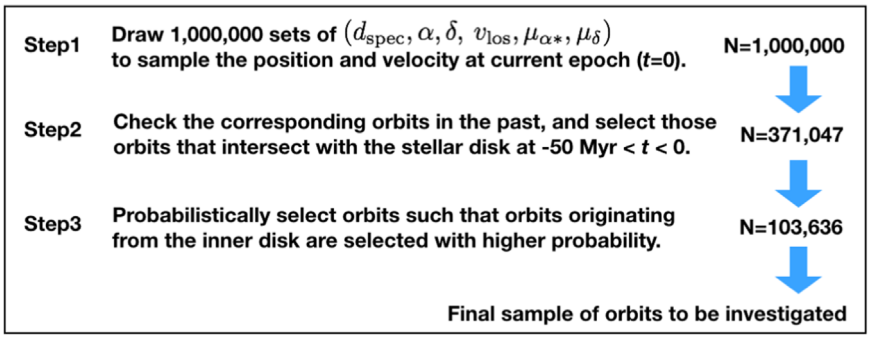

Figure 2. A flow chart that describes how we construct sample orbits from the error distribution.

classification, we provide additional lines of evidence (Section 3.3.1) and argue that LAMOST-HVS1 is not a hot blue horizontal-branch star (BHB star; $\lesssim 1\,M_\odot$). We note that some horizontal-branch stars extended beyond $T_{\rm eff} > 20000$ K are often classified as hot subdwarfs (Greenstein & Sargent 1974; Heber 2009); however, the detailed definition of BHB stars is not important in this paper.

3.3.1. Evidence that LAMOST-HVS1 is Not a BHB Star

Our analysis suggests that LAMOST-HVS1 shows $(T_{\rm eff}, \log g) = (18100 \pm 400\,{\rm K},\ 3.42 \pm 0.065)$. These values are inconsistent with a BHB star. The surface gravity for a BHB star as hot as LAMOST-HVS1 is about $\log g \simeq 4.6 \pm 0.2$, while a BHB star with $\log g \simeq 3.42$ has $T_{\rm eff} \simeq 10{,}000$ K (Dorman et al. 1993; Moni Bidin et al. 2007, 2011).

Our measurement of large projected rotational velocity, $v\sin(i) = 130\,{\rm km\,s^{-1}}$, of LAMOST-HVS1 is typical of massive stars. In contrast, hot BHB stars with $T_{\rm eff} > 11500$ K show slow rotation with $v\sin(i) < 7\,{\rm km\,s^{-1}}$ (Behr et al. 2000).

In addition, a hot BHB star with $T_{\rm eff} > 11500$ K shows a depleted helium abundance of $Y = {\rm He/H} \lesssim 10^{-2}$ (Behr et al. 1999; Moni Bidin et al. 2007), which is probably due to the diffusion (gravitational settling) of helium in the atmosphere (Greenstein 1967; Michaud et al. 1983, 2015). In contrast, the helium abundance of LAMOST-HVS1 is consistent with solar abundance.

Furthermore, the effective temperature and the metal abundance of this star are inconsistent with the assumption that this star is a BHB star. If this is a BHB star, then the intrinsic overall metallicity [M/H] has to be as metal-poor as [M/H] < -1 (Xue et al. 2008) because a metal-rich horizontal-branch star is necessarily red (Sandage & Wallerstein 1960; Lee et al. 1994; Gratton et al. 2010). In contrast, the intrinsic overall metallicity estimated from [Mg/H] and [Si/H], which are insensitive to $T_{\rm eff}$ or the internal evolution of a horizontal-branch star (Glaspey et al. 1989; Behr et al. 1999; Behr 2003; Moehler et al. 2003; Gratton et al. 2004; Fabbian et al. 2005), is super-solar ([Mg/H] $= 0.33 \pm 0.10$ and [Si/H] $= 0.60 \pm 0.06$ if we adopt the solar abundance from Asplund et al. 2009). Therefore it is highly unlikely that this star is a BHB star.

Based on these considerations, we claim that LAMOST-HVS1 is indeed a massive B-type subgiant star, confirming previous claims (Zheng et al. 2014; Huang et al. 2017; Hattori et al. 2018b).

4. Analysis of the Orbit of LAMOST-HVS1

4.1. Coordinate System and the Model Potential

We adopt a Galactocentric inertial right-handed Cartesian coordinate system (x, y, z), such that (x, y)-plane is the Galactic disk plane and z-axis is directed toward the North Galactic Pole. We assume that the Sun is on the Galactic plane $z = 0$ (Bovy 2017), and that the position of the Sun is $(x, y) = (-R_0, 0)$ with $R_0 = 8.0$ kpc. In addition, we define a Galactocentric cylindrical coordinate system (R, ϕ, z) such that $(x, y) = R\cos\phi, R\sin\phi)$.

We assume that the circular velocity at the solar position is $v_0 = 220\,{\rm km\,s^{-1}}$ (Kerr & Lynden-Bell 1986) and the solar peculiar velocity relative to the circular velocity is $(U_\odot, V_\odot, W_\odot) = (11.1,\ 12.24,\ 7.25)\,{\rm km\,s^{-1}}$ (Schönrich et al. 2010). We adopt a realistic Galactic potential model, `MWPotential2014` (Bovy 2015). We note that `MWPotential2014` model uses a spherical NFW dark matter halo with scale length $a = 16$ kpc, virial radius $r_{200} = 183$ kpc, and virial mass $M_{200} = 0.7 \times 10^{12}\,M_\odot$. However, the result of this paper is not sensitive to the adopted virial mass M_{200}, as long as a and $r_{\rm vir}$ are tuned so that the rotation curve is almost unchanged. For example, by taking into account that recent measurements of M_{200} of the Milky Way based on *Gaia* DR2 (e.g., Posti & Helmi 2019; Watkins et al. 2019; see also Hattori et al. 2018a) is $\sim$2 times more massive than that of `MWPotential2014`, we have checked that the result of this paper is unchanged when we adopt $(a, r_{200}, M_{200}) = (28$ kpc, 231 kpc, $1.4 \times 10^{12}\,M_\odot)$.

4.2. Sample Orbits that Represent the Observational Uncertainty of LAMOST-HVS1's Orbit

In reconstructing the orbit of LAMOST-HVS1, we have to take into account the observational uncertainties in the current position and the velocity of the star. As mentioned in Section 2, we believe that LAMOST-HVS1 is a young star that was recently ejected from the stellar disk. Thus, this prior belief should also be considered in reconstructing the orbit. To this end, we use a Monte Carlo approach, as summarized in the flow chart in Figure 2. In the following, we describe our approach in more detail.

To handle the observational uncertainty, we draw 1,000,000 sets of the observed 6D position–velocity, $(d_{\rm spec}, \alpha, \delta, v_{\rm los}, \mu_{\alpha*}, \mu_\delta)$, from the observed values of these quantities and their associated error distributions. Here, we fully take into account the correlation between $\mu_{\alpha*}$ and μ_δ, but we ignore the tiny errors on (α, δ).

Each realization of a 6D observable vector is converted to the Cartesian position (x, y, z) and velocity (v_x, v_y, v_z) at the current epoch, $t = 0$. This information is then used to compute the corresponding orbit in the past, at $-T_{\rm int} < t < 0$. Here, we adopt a conservatively long integration time $T_{\rm int} = 50\,{\rm Myr}$, which is longer than our spectroscopic age estimate of $\tau = 37\,{\rm Myr}$. We adopted this value of $T_{\rm int}$, so that systematic error on τ does not seriously affect our results.

For 628,953 of the 1,000,000 realizations (63%), the corresponding orbit does not intersect with the disk plane at $-T_{\rm int} < t < 0$. We discard these improbable orbits and we consider the remaining 371,047 orbits (37%) in the following calculation. For each of these 371,047 orbits, we record the epoch $t = -T_{\rm flight}$ when the orbit intersects with the disk plane. This time is interpreted as the epoch when LAMOST-HVS1 was ejected from the stellar disk, and $T_{\rm flight}$ corresponds to the flight time of the LAMOST-HVS1 after ejection. We also record the Galactocentric position $(x_{\rm ej}, y_{\rm ej}, z_{\rm ej} = 0)$ and Galactic rest-frame velocity $(v_{{\rm ej},x}, v_{{\rm ej},y}, v_{{\rm ej},z})$ at the ejection epoch. In addition, we record the intrinsic ejection velocity

$$\begin{aligned} \boldsymbol{V}_{\rm ej}^{\rm int} &= (V_{{\rm ej},x}^{\rm int}, V_{{\rm ej},y}^{\rm int}, V_{{\rm ej},z}^{\rm int}) \\ &= (v_{{\rm ej},x}, v_{{\rm ej},y}, v_{{\rm ej},z}) - (v_{\rm circ}\sin\phi_{\rm ej}, \\ &\quad - v_{\rm circ}\cos\phi_{\rm ej}, 0) \end{aligned} \tag{2}$$

which is measured with respect to the local circular velocity. The magnitude of the intrinsic ejection velocity $V_{\rm ej}^{\rm int} = |\boldsymbol{V}_{\rm ej}^{\rm int}|$ can be regarded as the impulsive velocity change that LAMOST-HVS1 experienced when it was ejected from the stellar disk, with an assumption that it was orbiting in the Milky Way in a circular orbit before the ejection. Here, $v_{\rm circ}$ is the circular velocity in our potential model evaluated at the Galactocentric cylindrical radius $R_{\rm ej}$; and we note $(x_{\rm ej}, y_{\rm ej}) = (R_{\rm ej}\cos\phi_{\rm ej}, R_{\rm ej}\sin\phi_{\rm ej})$.

As discussed earlier, LAMOST-HVS1 is a massive B star that was probably ejected from the stellar disk. Thus, our initial guess (prior to the detailed orbital analysis) on the probability distribution of the ejection location of this star, $(x_{\rm ej}, y_{\rm ej}, z_{\rm ej})$, is proportional to the density distribution of massive B-type stars in the disk. To take this prior distribution into account, we randomly draw 103,636 orbits from the 371,047 orbits according to a probability that is proportional to[7] $\Sigma(R_{\rm ej}) \propto \exp[-R_{\rm ej}/(2.5\,{\rm kpc})]$. Here, we adopt this functional form of $\Sigma(R)$ by taking into account the observed surface density of thin disk stars (Yoshii 2013). Although this weighting scheme is simple, we find it useful because it does not require any knowledge on the dynamical process that ejected this star. In Section 5, we will analyze these 103,636 orbits.

4.3. Caveat

In Section 4.2, we discard 63% of the realized Monte Carlo orbits because they have not recently crossed the disk plane (in the last 50 Myr). We think that this is mainly because our spectroscopic distance is not accurate enough (see Section 5.1). More reliable parallax data from future data releases of *Gaia* would be helpful to check this view. If our spectroscopic distance and age are correct (and if the *Gaia* proper motion is correct—see Appendix), then the tension between the flight time and the stellar age might indicate a possibility that LAMOST-HVS1 did not originate from the Galactic disk. However, the chemical abundance pattern is consistent with the disk origin of this star (see Table 2 and Section 5.7), so we do not pursue this unlikely possibility further in this paper.

[7] A more appropriate prior should be proportional to $\rho(x_{\rm ej}, y_{\rm ej}, z_{\rm ej}) \propto \exp[-R_{\rm ej}/(2.5\,{\rm kpc})]\exp[-|z_{\rm ej}|/z_d]$ with z_d the scale height of B stars. Our assumption is equivalent to setting $z_d \to +0$, respecting the high concentration of B stars on the disk plane.

5. Result: Properties of the Reconstructed Orbit of LAMOST-HVS1

In Figure 3, we plot the distributions of various quantities characterizing the ensemble of 103,636 reconstructed orbits for LAMOST-HVS1. This plot summarizes the most important results of this paper. Based on our orbital analysis, LAMOST-HVS1 is currently located $d \simeq 13\,{\rm kpc}$ away from the Sun, it was ejected from the stellar disk about $T_{\rm flight} \simeq 33\,{\rm Myr}$ ago, its ejection location was in the inner disk ($R_{\rm ej} \simeq 3\,{\rm kpc}$) and it was ejected with an initial intrinsic speed of $V_{\rm ej}^{\rm int} \simeq 568\,{\rm km\,s^{-1}}$ (magnitude of the velocity vector defined in Equation (2)). In what follows, we investigate the physical implications of these results.

5.1. Heliocentric Distance to LAMOST-HVS1

Figure 3 shows the probability distributions of various quantities $(V_{\rm ej}^{\rm int}, R_{\rm ej}, T_{\rm flight}, d)$ associated with the 103,636 orbits. We note that the distributions of various quantities, especially $(R_{\rm ej}, T_{\rm flight}, d)$, are highly correlated. These correlations are, in fact, almost entirely explained by the distance uncertainty because the observational uncertainty of the current position and velocity of LAMOST-HVS1 is dominated by the distance uncertainty. Thus, we first investigate the heliocentric distance to LAMOST-HVS1 and demonstrate that our orbital analysis actually improves our estimate on the distance to this star.

The initial guess for the heliocentric distance was our spectroscopic distance estimate, $d_{\rm spec}$. The probability distribution of $d_{\rm spec}$, represented by the 1,000,000 Monte Carlo sample, is shown by the green-dashed histogram in Figure 4. As we can see, this distribution has a long tail toward large distance (up to $d_{\rm spec} \simeq 35\,{\rm kpc}$).

Our orbital analysis shows that only 371,047 orbits (37%) are consistent with the scenario that LAMOST-HVS1 was recently ejected from the stellar disk (less than 50 Myr ago). These orbits have relatively small heliocentric distance, $d \lesssim 17\,{\rm kpc}$, as we can see from the orange histogram in Figure 4. This preference toward small heliocentric distance is simply a consequence of requiring the flight time to be smaller than the upper limit (50 Myr).

After taking into account the probability distribution of the ejection radius $R_{\rm ej}$ arising from the stellar density profile of the disk, the distribution of d for our final sample of 103,636 orbits is even more weighted toward smaller values, as shown by the blue-thick histogram in Figure 4. Thus our estimate of the distance to this star is substantially improved by the information on the stellar orbit, our assumptions on the physical nature of the star, and properties of the stellar disk from which it was (assumed to be) ejected. Hereafter, we will only use this posterior distribution of the distance, $d = 13.4^{+1.7}_{-1.5}\,{\rm kpc}$. We note that this estimate happens to be close to the estimate by Zheng et al. (2014).

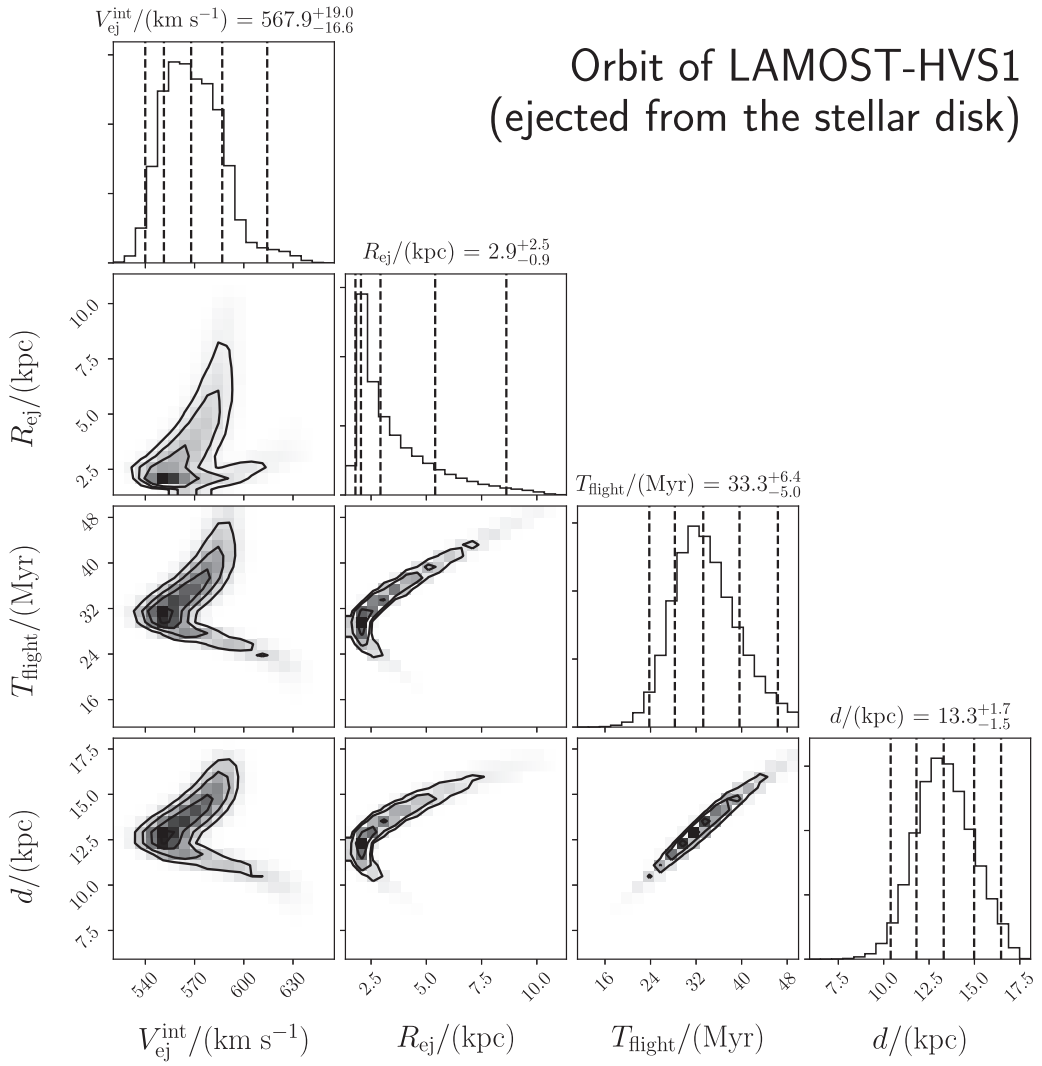

Figure 3. The probability distribution of the orbital properties of LAMOST-HVS1 represented by 103,636 orbits sampled from our analysis. The uncertainty in these orbital parameters are almost exclusively explained by the distance uncertainty, as described in Section 5.1. The dashed vertical lines in the histograms represent the 2.5th, 16th, 50th, 84th, and 97.5th percentiles of the distributions.

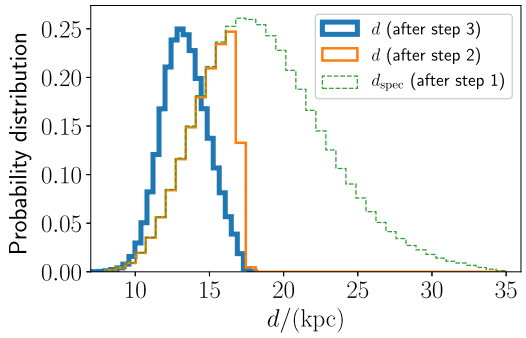

Figure 4. The probability distribution of the distance to LAMOST-HVS1. The distance distribution of the sampled orbits after (step 1), (step 2), and (step 3) in Figure 2 are shown by the green dashed, orange thin, and blue thick histograms, respectively. We see that the spectroscopic distance (green-dashed histogram) is comparatively uncertain by itself, and our belief in the distance is improved after we take into account the orbital information (blue-solid histogram). The blue-thick and orange-thin histograms are normalized to unity; while the green-dashed histogram is scaled so that the difference from the orange-thin histogram can be clearly seen.

5.2. Current Position and Velocity of LAMOST-HVS1

The orbital analysis also improves our guess on the 3D position and velocity of LAMOST-HVS1. Based on the current position of the 103,636 orbits, we estimate that LAMOST-HVS1 is currently located at $(x, y, z) = (-16.2^{+0.9}_{-1.0}, -7.1^{+0.8}_{-0.9}, 7.7^{+1.0}_{-0.9})$ kpc (see Figures 5(a) and (b)) with a velocity of $(v_x, v_y, v_z) = (-504^{+16}_{-18}, -131^{+7}_{-7}, 187^{+20}_{-22})$ km s^{-1}. We note that the current total velocity is $v = 553^{+11}_{-9}$ km s^{-1}, which makes this star one of the highest-velocity massive stars currently known in the Milky Way (see Zheng et al. 2014; Brown 2015; Huang et al. 2017; Erkal et al. 2019; Hattori et al. 2018a; Li et al. 2018; Marchetti et al. 2018). Based on these estimated phase space coordinates, the angular momentum of this star is $(L_x, L_y, L_z) = (-329^{+178}_{-122}, -852^{+671}_{-824}, -1474^{+335}_{-400})$ kpc km s^{-1}. We note that the value of azimuthal angular momentum L_z is substantially different from zero, which suggests that LAMOST-HVS1 was not ejected by the SMBH at the Galactic Center. Also, the prograde orbit ($L_z < 0$)

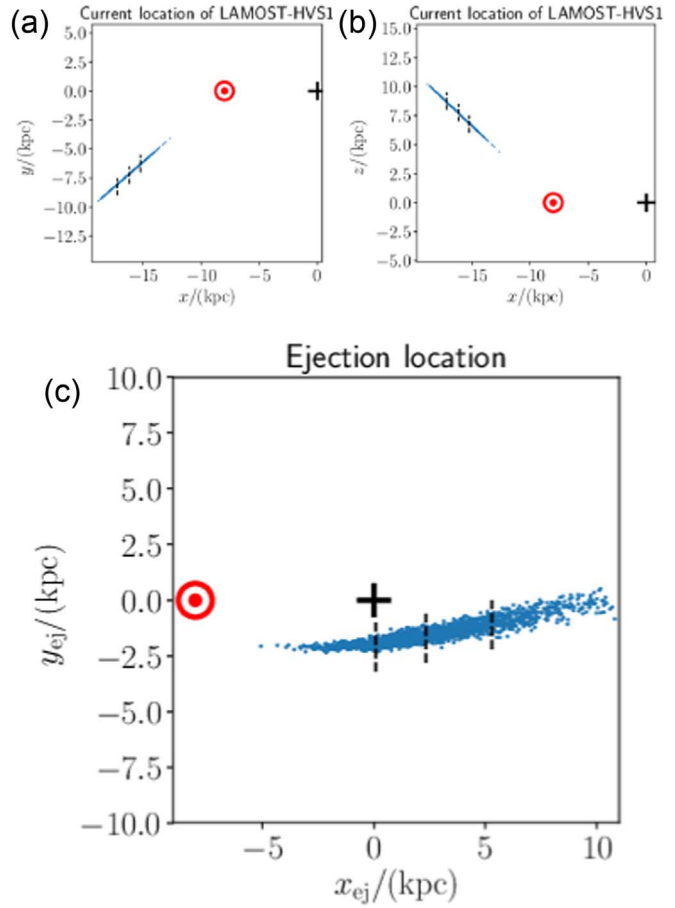

Figure 5. The probability distribution of the current location of LAMOST-HVS1 (upper two panels) and the location when it was ejected from the stellar disk (bottom panel) represented by the 103,636 sample orbits. (Only 2% of them are shown for clarity.) The black plus and red dot correspond to the Galactic Center and the current solar position, respectively. In panels (a) and (b), the vertical dashed lines indicates the 16th, 50th, and 84th percentiles of the current x coordinate of LAMOST-HVS1, which are shown to provide a rough idea of the distance uncertainty. In panel (c), the vertical dashed lines indicate the 16th, 50th, and 84th percentiles of the x coordinate of the ejection location, x_{ej}.

of this star supports the view that LAMOST-HVS1 was ejected from the stellar disk.

5.3. Flight Time T_{flight} of LAMOST-HVS1

The orbital analysis suggests that the flight time of LAMOST-HVS1 after it was ejected from the stellar disk is $T_{flight} = 33.3^{+6.4}_{-5.0}$ Myr (see Figure 3). It is reassuring that the median flight time (33.3 Myr) is smaller than the median spectroscopic age τ ($\simeq$37 Myr) (note that the spectroscopic age was not a constraint on the orbits, rather we required flight times to be less than 50 Myr). The proximity of the stellar age to the flight time is intriguing, suggesting that LAMOST-HVS1 must have been ejected just after it was born if we adopt our estimate of its spectroscopic age at face value.

5.4. Ejection Location of LAMOST-HVS1

Figure 5(c) shows the distribution of the ejection locations (x_{ej}, y_{ej}) for the ensemble of 103,636 orbits (small blue dots). The location of the Galactic Center (black +) and the current location of the Sun (red $\odot$) are also marked. The Galactocentric radius of the ejection location is $R_{ej} = 2.9^{+2.5}_{-0.9}$ kpc (see also Figure 3), where the star formation has been very active recently (Messineo et al. 2016). The chemical abundance of LAMOST-HVS1 is consistent with the view that this star was ejected from the inner stellar disk (see Table 2 and Section 5.7).

As seen from Figure 5(c), the distribution of (x_{ej}, y_{ej}) is highly elongated. This elongated shape is almost exclusively explained by the uncertainty in the current heliocentric distance to LAMOST-HVS1. The ejection position (x_{ej}, y_{ej}) of a sample orbit with smaller (larger) value of x_{ej} corresponds to smaller (larger) current heliocentric distance.

As shown in Figure 3, the heliocentric distance d and the flight time T_{flight} are almost linearly correlated. Similarly, we found that x_{ej} and T_{flight} are almost linearly dependent. In Figure 5(c), an orbit with $x_{ej} \simeq -4.7$ kpc has $T_{flight} \simeq 16.7$ Myr, while an orbit with $x_{ej} \simeq 11$ kpc has $T_{flight} \simeq 50$ Myr (the maximum allowed flight time). There are no sampled orbits with $x_{ej} > 11.4$ kpc due to our limit on T_{flight}.

The Galactocentric radius of the ejection location $R_{ej} = \sqrt{x_{ej}^2 + y_{ej}^2}$ attains its minimum when $d \simeq 12$ kpc (and $x_{ej} \simeq 0$ kpc). The value of R_{ej} becomes larger for $d < 12$ kpc and $d > 12$ kpc since $|x_{ej}|$ becomes larger (while y_{ej} varies only mildly as a function of d). This is why we see a "L"-shaped correlation between R_{ej} and d in Figure 3.

5.5. Intrinsic Ejection Velocity of LAMOST-HVS1

Given the current position and velocity of LAMOST-HVS1, the x-component of its velocity $v_{ej,x}$ just after the ejection must have been a large negative value. If LAMOST-HVS1 had a circular orbit before the ejection, then the intrinsic ejection velocity V_{ej}^{int} is smallest when the velocity vector of the circular orbit is most closely aligned with the velocity just after the ejection, ($v_{ej,x}$, $v_{ej,y}$, $v_{ej,z}$). This minimum value of V_{ej}^{int} is attained when $x_{ej} \simeq 1.5$ kpc and $R_{ej} \simeq 2.2$ kpc. This is the reason for the "L"-shaped correlation between R_{ej} and V_{ej}^{int} in Figure 3.

It is important to note that even in the extreme case when the intrinsic ejection velocity $\boldsymbol{V}_{ej}^{int}$ is most closely aligned to the circular orbit rotating with the circular velocity of the disk at that radius, the magnitude of V_{ej}^{int} is as large as 530 km s^{-1}. The intrinsic ejection velocity of $V_{ej}^{int} \simeq 568^{+19}_{-17}$ km s^{-1} is much larger than those of other massive B-type runaway stars (see Sections 5.5.1 and 5.5.2).

5.5.1. Comparison with Nearby Massive Runaway Stars in Silva & Napiwotzki (2011)

To demonstrate that the massive runaway star LAMOST-HVS1 is exceptional in its large V_{ej}^{int}, we also analyzed known runaway B-type massive stars in Silva & Napiwotzki (2011), who analyzed the orbits of 96 stars that they classified as main-sequence stars. We found that *Gaia* data is available for all of these stars. For the 46 stars in this sample with high quality parallax data ($\varpi/\sigma_\varpi > 5$), we derived the probability distribution of V_{ej}^{int}, and derived the 16th, 50th, and 84th percentile values of V_{ej}^{int}. We found that only three stars (HIP 114569, HIP 11809, PG 1533+467) have V_{ej}^{int} that is consistent with 300 km s^{-1} or larger (i.e., the 84th percentile value of V_{ej}^{int} is larger than 300 km s^{-1}). Figure 6 shows the probability

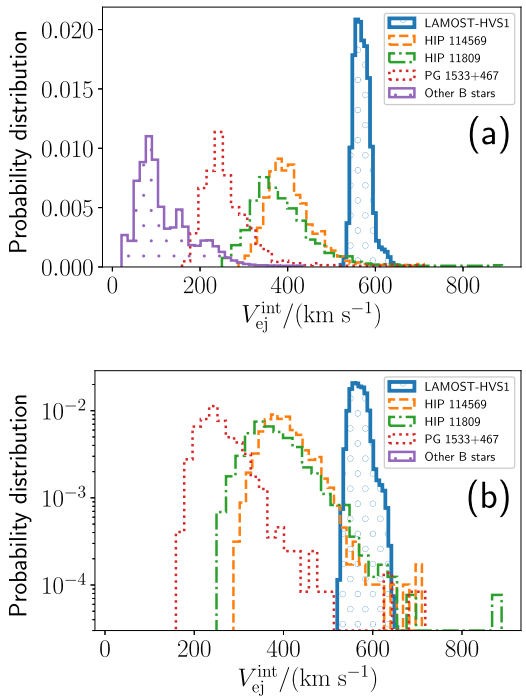

Figure 6. The probability distribution of the ejected velocity for LAMOST-HVS1 and 46 other runaway stars in Silva & Napiwotzki (2011) with good *Gaia* parallaxes. For clarity, we show the same histograms in linear and logarithmic scales on top and bottom panels, respectively.

distribution of $V_{\rm ej}^{\rm int}$ for these three stars. We also show the combined probability distribution of $V_{\rm ej}^{\rm int}$ for the remaining 43 high-quality sample. From this figure, we see that $V_{\rm ej}^{\rm int}$ of LAMOST-HVS1 is much larger than that of any other nearby massive B-type runaway stars with high-quality parallax.

We note that the sample in Silva & Napiwotzki (2011) includes some stars that are several kpc away from the Galactic disk according to their spectroscopic distance. Since our cut on the fractional error in parallax (ϖ/σ_ϖ) preferentially excludes distant stars, some of these distant runaway stars might have a very large $V_{\rm ej}^{\rm int}$. However, because the main focus of this paper is LAMOST-HVS1, we do not pursue this point in this paper.

5.5.2. Comparison with Other Fast-moving Stars

Prior to *Gaia* DR2, more than 20 hypervelocity star candidates have been studied (Brown 2015; Huang et al. 2017). The re-analysis of these stars after *Gaia* DR2 shows that some fraction of them are probably runaway stars that have been ejected from the Galactic disk (Brown et al. 2018; Erkal et al. 2019; Irrgang et al. 2018). Most of these stars are late B-type or A-type main-sequence stars with $M \lesssim 4\,M_\odot$ (Brown et al. 2014), and only a few of them are as massive as LAMOST-HVS1.

For example, HD 271791 is a 11 $M_\odot$ runaway star that was ejected from the outskirt of the Galactic stellar disk (Heber et al. 2008). Due to its large current velocity, HD 271791 is classified as a hyper-runaway star. However, we have confirmed based on the *Gaia*-DR2 proper motion data that the intrinsic ejection velocity of HD 271791 is $V_{\rm ej}^{\rm int} \simeq 400\ {\rm km\ s^{-1}}$, which is not as large as that of LAMOST-HVS1.

In addition, an early B-type star LAMOST-HVS2 (Huang et al. 2017) is a good candidate for a massive hyper-runaway star. Our (unpublished) preliminary analysis suggests that this star has a high probability of having been ejected from the Galactic stellar disk, which is consistent with Erkal et al.'s (2019) study. However, due to the lack of high-resolution spectrum of this star, we cannot rule out the possibility that this star is a low-mass blue star.

HIP 60350 is another example of high-velocity runaway star, but this star is only 4.9 $M_\odot$ (Irrgang et al. 2010) and is not as massive as LAMOST-HVS1. Li et al. (2018) discovered a hyper-runaway candidate (LAMOST-HVS4), but this star is only $\sim$4 $M_\odot$ if it is a main-sequence star. There is also a possibility that this star is a low-mass BHB star due to the low-resolution spectra currently available for this star.

Although HVS3 (HE 0437-5439) is as massive as LAMOST-HVS1, it may have originated from the Large Magellanic Cloud (Edelmann et al. 2005; Gualandris & Portegies Zwart 2007; Bonanos et al. 2008; Przybilla et al. 2008; Brown 2015; Erkal et al. 2019; Irrgang et al. 2018).

Based on these considerations, we argue that LAMOST-HVS1 is the only well-confirmed massive hyper-runaway star that has been ejected from the Galactic stellar disk with an extremely large intrinsic ejection velocity of $V_{\rm ej}^{\rm int} \sim 600\ {\rm km\ s^{-1}}$.

5.6. Current Location of the Ejection Agent of LAMOST-HVS1

Theoretical investigations have suggested some possible mechanisms that accelerate disk stars to produce runaway stars with extreme velocity. In all of these mechanisms, a nearby object—including IMBH or VMS—plays an important dynamical role in ejecting a disk star. To date, there is no conclusive evidence that an IMBH exists in the Milky Way (although there have been claims of objects close to the central SMBH; e.g., Oka et al. 2017). While a few VMSs have been discovered (e.g., the initial mass of Pistol star is estimated to be 200–250 $M_\odot$; Figer et al. 1998), there is no consensus on the numbers of such stars that exist in the Galaxy and under what specific conditions they form. Thus, there are compelling reasons to investigate the current location of the "ejection agent" for LAMOST-HVS1 (the object that took part in the ejection of LAMOST-HVS1).

Since the ejection agent was located at ($x_{\rm ej}$, $y_{\rm ej}$, 0) at $t = -T_{\rm flight}$, we can derive its current position by assuming the velocity at $t = -T_{\rm flight}$ and integrating the orbit in our model potential (Section 4.1) until $t = 0$. For each of the 103,636 sample orbits, we assume that the velocity of the ejection agent at $t = -T_{\rm flight}$ is given by $(v_x, v_y, v_z) = (v_{\rm circ}\sin\phi_{\rm ej} + v_{{\rm pec},x}, -v_{\rm circ}\cos\phi_{\rm ej} + v_{{\rm pec},y}, 0)$. Here, the peculiar velocity (deviation from the circular velocity) $v_{{\rm pec},x}$ and $v_{{\rm pec},y}$ are randomly drawn from a 2D isotropic Gaussian distribution with a dispersion of 20 km s^{-1} (typical of the velocity dispersion of young stars in the Milky Way). We note that the orbit of the ejection agent is assumed to be confined to the Galactic disk plane.

Figure 7(a) shows (in blue dots) the possible current location of the ejection agent in the Galactic plane represented by the 103,636 Monte Carlo samples. To guide the eye, we draw three dashed lines that correspond to the 16th, 50th, and 84th percentile values of probable Galactic longitude of the ejection agent. The curved solid lines of various colors represent the current positions of the known prominent spiral arms: Norma (magenta), Perseus (yellow), Sagittarius-Carina (green) and

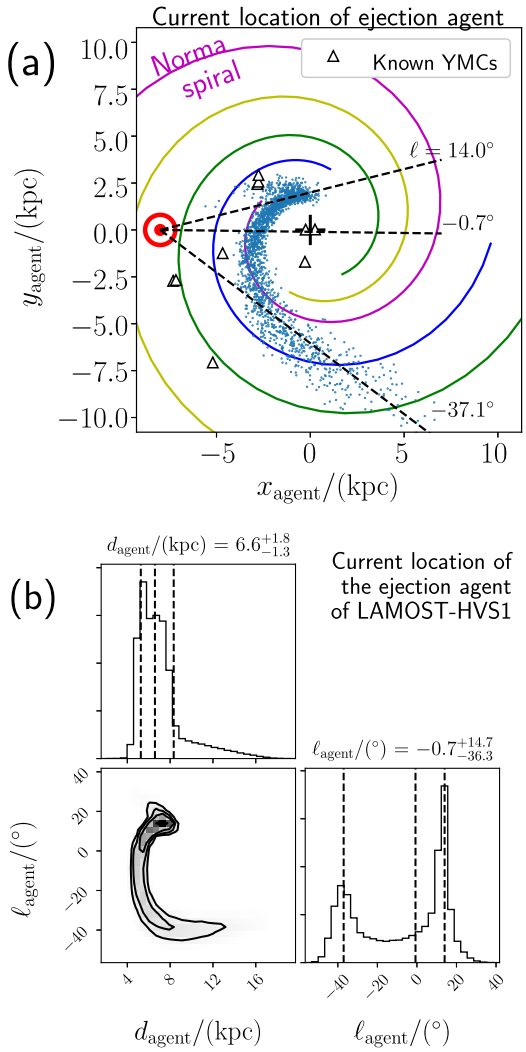

Figure 7. The probability distribution of the current position of the ejection agent of LAMOST-HVS1 (the object that ejected LAMOST-HVS1; this may be an IMBH, a VMS, or ordinary massive stars in the natal star cluster). (a) The distribution in the Galactic disk plane is represented by the 103,636 Monte Carlo sample. (Only 2% of them are shown for clarity.) We note that the spatially elongated distribution arises from the uncertainty in the current heliocentric distance to LAMOST-HVS1. The distribution appears to have a significant overlap with the Norma spiral arm. The three dashed lines indicate the 16th, 50th, and 84th percentiles of the Galactic longitude. The open triangles show the locations of the known young massive clusters (Portegies Zwart et al. 2010). (b) This panel shows the same information, but in the distance ($d_{\rm agent}$) and Galactic longitude ($\ell_{\rm agent}$) space. The three vertical dashed lines in the bottom right panel indicate the 16th, 50th, and 84th percentiles of the Galactic longitude, which are also shown in panel (a).

Scutum-Cruz (blue) (Vallée 2008). From this figure, we see that the probability distribution of the current location of the ejection agent has an elongated shape, reflecting the elongated distribution of ($x_{\rm ej}$, $y_{\rm ej}$). We also note that this elongated distribution is bent at a dashed line of $\ell = 14.^\circ0$. This structure is due to the differential rotation of the disk. Since the angular velocity of disk stars is larger at smaller R, the ejection agents with smaller $R_{\rm ej}$ rotate around the Milky Way at a larger angular velocity. We also note that the Monte Carlo points (blue dots) are nearly aligned with the Norma spiral arm (magenta curve) at $-37.^\circ1 < \ell < 14.^\circ0$, which corresponds to the central 68% of the distribution. This is consistent with the idea that young massive star clusters, where massive stars are thought to form, are expected to be located in or close to spiral arms.

Figure 7(b) shows the probability distributions for the current location of the ejection agent in the ($d_{\rm agent}$, $\ell_{\rm agent}$)-plane. We see that the Galactic longitude $\ell_{\rm agent}$ has a wide distribution with two prominent peaks. These peaks happen to be located near the 84th and 16th percentiles of $\ell_{\rm agent}$, at $\ell_{\rm agent} = 14.^\circ0$ and $-37.^\circ1$. One of the peaks at $\ell_{\rm agent} = 14.^\circ0$ approximately corresponds to the bending point of ($x_{\rm agent}$, $y_{\rm agent}$). We found that 20% of the orbits in the distribution are enclosed at $11.^\circ8 < \ell_{\rm agent} < 15.^\circ4$, and the corresponding heliocentric distance at this longitude range is $7.2^{+0.6}_{-0.7}$ kpc. Another peak at $\ell_{\rm agent} = -37.^\circ1$ corresponds to the tail of the distribution at $y_{\rm agent} < -4$ kpc, whose distribution is nearly aligned with the line of $\ell_{\rm agent} = -37.^\circ1$.

5.6.1. LAMOST-HVS1 Indicates an Undiscovered Young Massive Cluster (YMC)?

In the above calculation, we have implicitly assumed that the ejection agent still survives until today. This is probably the case if the ejection agent is an IMBH, but it is not the case if it is a reasonably massive star ($\gtrsim$30 $M_\odot$) due to the supernova explosion. Even if the ejection agent does not survive until today, our calculation is still useful because it shows the current location of the natal star cluster of LAMOST-HVS1.

If the natal cluster of LAMOST-HVS1 is as massive as 10^4 $M_\odot$ (which is a reasonable assumption as we will describe in Sections 6 and 7) located at $R \sim 3$ kpc, then the cluster can survive for $\sim$1 Gyr according to Equation (19) of Portegies Zwart et al. (2010). Even if the cluster mass is $\sim 10^3$ $M_\odot$, then it survives for $\sim$200 Myr. This means that the natal cluster may well survive until today. As shown in Figure 7(a), only three YMCs (RSGC1, RSGC2, and RSGC3) at around (x, y) = (-2.8, 2.5) kpc are marginally consistent with the region where the natal cluster of LAMOST-HVS1 can be located. However, since RSGC1-3 are only 12–18 Myr old (Portegies Zwart et al. 2010), these clusters did not exist when LAMOST-HVS1 was ejected (about 33 Myr ago). Moreover, the sub-solar abundance of O, Mg, and Si of RSGC1-3 (Davies et al. 2009; Origlia et al. 2016) is also inconsistent with the super-solar abundance of these elements for LAMOST-HVS1. Therefore, none of the known YMCs could have ejected LAMOST-HVS1. This result indicates that the natal cluster of LAMOST-HVS1 is an undiscovered YMC probably located along the Norma spiral arm (which may be heavily dust obscured). The chemical abundance pattern of LAMOST-HVS1 (see Table 2) might be useful to identify its natal YMC or its sibling stars that were born in the same cluster. This "chemical-tagging" (Freeman & Bland-Hawthorn 2002; Hawkins & Wyse 2018) may help our understanding on the origin of hyper-runaway stars.

5.7. Chemistry of LAMOST-HVS1

As we have shown, the kinematic data of LAMOST-HVS1 indicate that it was ejected from the inner stellar disk. Here we show that its chemical data are consistent with this view.

Young stars in the Galactic disk (e.g., classical Cepheids and OB stars) are known to have a negative abundance gradient such that the inner stellar disk is more metal-rich than in the outer disk (Carigi et al. 2005; Esteban et al. 2005; Cescutti et al. 2007). As seen in Table 2, the abundance of Mg, C, N, and O of LAMOST-HVS1 is systematically higher than that of the

mean abundance $\langle A_{\rm B}^{8\,{\rm kpc}}\rangle$ of B stars at $R = 8$ kpc, while it is consistent with $\langle A_{\rm B}^{3\,{\rm kpc}}\rangle$ at $R = 3$ kpc. The similarity in the chemical abundance pattern between LAMOST-HVS1 and B stars at $R = 3$ kpc supports our estimation that the ejection radius of LAMOST-HVS1 was at $R_{\rm ej} = 2.9^{+2.5}_{-0.9}$ kpc.

The Si abundance of LAMOST-HVS1 is, in contrast, appreciably higher than that of typical B stars at $R = 3$ kpc. This excess of Si is intriguing because another α element Mg (whose origin is similar to that of Si) does not show such an excess. To see if the excess of Si is anomalous, we checked the relative abundance of Si and Mg, $A({\rm Si}) - A({\rm Mg})$, for Cepheids across the Galactic disk. To this end, we used 231 Cepheids in Luck & Lambert (2011), for which both [Si/H] and [Mg/H] are available. We used [Si/H] and [Mg/H] for these stars and Grevesse et al. (1996) solar abundance to derive $A({\rm Si}) - A({\rm Mg})$. We did not see a clear trend of $A({\rm Si}) - A({\rm Mg})$ as a function of R, and $A({\rm Si}) - A({\rm Mg})$ has the mean value of -0.01 and the standard deviation of 0.13. Among these 231 Cepheids, we found 10 stars that show $A({\rm Si}) - A({\rm Mg}) > 0.18$, and three stars with $A({\rm Si}) - A({\rm Mg}) > 0.30$. Thus, the observed $A({\rm Si}) - A({\rm Mg}) = 0.18 \pm 0.10$ for LAMOST-HVS1 may not be exceptionally high.[8] The excess of Si for LAMOST-HVS1 might be helpful to identify its natal star cluster or its sibling stars (see Section 5.6.1).

6. Ejection Mechanism of LAMOST-HVS1

As reviewed in Section 1, there are two possible mechanisms to eject a runaway star—BEM and DEM. Here, we investigate which of these mechanisms could be responsible for the hyper-runaway star LAMOST-HVS1.

6.1. Binary Ejection Mechanism (BEM)

In BEM, the intrinsic ejection velocity of a runaway star that is as massive as LAMOST-HVS1 ($M \simeq 8\,M_\odot$) is expected to be smaller than $\sim$400 km s^{-1} (see Section 1). This upper limit is significantly smaller than the ejection velocity $V_{\rm ej}^{\rm int} \simeq 568^{+19}_{-17}$ km s^{-1} of LAMOST-HVS1. Thus, BEM is disfavored by our estimate of $V_{\rm ej}^{\rm int}$.

6.2. Dynamical Ejection Mechanism (DEM)

In DEM, the intrinsic ejection velocity can be as large as $V_{\rm ej}^{\rm int} \sim 10^3$ km s^{-1}, depending on the situation (see references in Section 1). Thus, our estimate of the ejection velocity for LAMOST-HVS1 is compatible with DEM. Here, we further investigate the required situation for realizing the ejection velocity of LAMOST-HVS1.

6.2.1. Three-body Interaction Including an IMBH

The Hills mechanism is a dynamical mechanism in which a massive compact object (e.g., a black hole) captures one star in a stellar binary that passes nearby and ejects the other star with a large velocity (Hills 1988; Yu & Tremaine 2003). Gualandris & Portegies Zwart (2007) and Gvaramadze et al. (2008) investigated how an IMBH ejects an $8\,M_\odot$ main-sequence star with Hills mechanism. Their works are useful for us because LAMOST-HVS1 is also $\simeq 8\,M_\odot$. They estimated the probability that an $8\,M_\odot$ star attains $V_{\rm ej}^{\rm int} > 500$ km s^{-1} during this process. They found that this probability is larger: (i) if the IMBH is more massive; (ii) if the binary companion of the $8\,M_\odot$ star is more massive; or (iii) if the initial orbital separation a of the binary is smaller (more compact binary). For example, when an equal-mass binary consisting of two $8\,M_\odot$ stars interacts with an IMBH with $M_{\rm BH} = 10^2\,M_\odot$, there is $\sim$1% probability that one of the $8\,M_\odot$ star attains larger ejection velocity than LAMOST-HVS1. This probability increases to $\sim$15% and $\sim$30%, if $M_{\rm BH} = 10^3\,M_\odot$ and $10^4\,M_\odot$, respectively. Thus, this mechanism can explain the ejection of LAMOST-HVS1.

If LAMOST-HVS1 was ejected by an IMBH, then we expect that this IMBH is currently located at the region shown in Figure 7. If this hypothetical IMBH captures a nearby star to form a close binary, then it may emit ultra-luminous X-rays ($>10^{39}$ erg s^{-1}) by accreting material from the binary companion (Hopman et al. 2004). There are no observational signatures of such ultra-luminous X-ray sources in that region (or elsewhere in the Milky Way). This may be explained: (i) if the hypothetical IMBH currently does not have a close binary companion; (ii) if the close binary companion has stopped transferring material to the IMBH; or (iii) if the X-ray source is highly obscured by dust. Even if the hypothetical IMBH does not have a close binary companion, it could emit (lower-luminosity) X-rays ($<10^{39}$ erg s^{-1}) from an accretion disk formed from ambient molecular gas in the natal cloud. These X-rays might have been already observed as an unclassified hard X-ray source on the Galactic disk plane (Fornasini et al. 2017; Krivonos et al. 2017; Oh et al. 2018). In this regard, it is interesting to note that Fornasini et al. (2017) published some ill-characterized X-ray sources in the Norma spiral arm region (such as the source named "NNR 28" in Fornasini et al. 2017).

6.2.2. Three-body Interaction Including a VMS (50–100 $M_\odot$ or More)

The Hills mechanism is effective not only around an IMBH but also around other massive compact objects, such as VMSs with a mass $M_{\rm VMS} = 50$–$100\,M_\odot$ or more. These stars may have formed as a result of runaway mergers of less massive stars in dense star clusters (Miller & Hamilton 2002; Portegies Zwart et al. 2004). The Pistol star in the Arches cluster, whose initial mass is estimated to be 200–250 $M_\odot$ (Figer et al. 1998), could be an example of such a star. Gvaramadze et al. (2009) showed that when a compact stellar binary with the initial separation of $a = 0.15$ au consisting of main-sequence stars with mass of ($8\,M_\odot$, $40\,M_\odot$) interacts with a $100\,M_\odot$ VMS, then the Hills mechanism ejects the $8\,M_\odot$ star with a velocity of $V_{\rm ej}^{\rm int} > 600$ km s^{-1} (similar to $V_{\rm ej}^{\rm int}$ of LAMOST-HVS1) with a probability of 1%. This probability is increased if $M_{\rm VMS}$ is larger and is decreased if a is larger, which are consistent with the similar results in Gualandris & Portegies Zwart (2007). Thus, the ejection of LAMOST-HVS1 can be explained with this mechanism.

6.2.3. Four-body Interaction Including a $\sim 30\,M_\odot$ Star

According to Table 1 of Leonard (1991), when two equal-mass binaries consisting of main-sequence stars with mass of (m, m) and ($4m$, $4m$) collide, the least massive star (m) can attain an ejection velocity up to $0.721 v_{{\rm esc},*}\,(4m)$, where $v_{{\rm esc},*}\,(4m)$ is the stellar surface escape velocity of the most massive star ($4m$).

[8] McEvoy et al. (2017) performed a non-LTE abundance analysis for 39 B-type runaway stars and found that 31 of them show $A({\rm Si}) - A({\rm Mg}) > 0$. This result indicates that the overabundance of Si over Mg may not be too peculiar for runaway stars.

If we set $m = 8\,M_\odot$, the corresponding ejection velocity of an $8\,M_\odot$ star is $770\,\mathrm{km\,s^{-1}}$ ($= 0.721 \times 1069\,\mathrm{km\,s^{-1}}$). (Here we assume the radius of a $32\,M_\odot$ star to be $10.7\,R_\odot$ following a 3 Myr old stellar model from Ekström et al. 2012.) This maximum ejection velocity is larger than our estimate of $V_{\rm ej}^{\rm int}$ for LAMOST-HVS1, so this mechanism can explain the ejection of this star.

6.2.4. Four-body Interaction with Stars with $8\,M_\odot$ or Less

Leonard (1991) claimed that when two identical equal-mass binaries consisting of main-sequence stars with mass of (m, m) and (m, m) collide, then one of the stars with mass m can attain an ejection velocity of up to $0.5 v_{\rm esc,*}$ (m). This upper limit remains the same or decreases if we replace some of the non-ejected stars with less massive stars. If we set $m = 8\,M_\odot$, then the corresponding ejection velocity of an $8\,M_\odot$ star is $477\,\mathrm{km\,s^{-1}}$ ($= 0.5 \times 954\,\mathrm{km\,s^{-1}}$). (Here we assume the radius of an $8\,M_\odot$ star to be $3.36\,R_\odot$ following Ekström et al. 2012.) This maximum ejection velocity is smaller than our estimate of $V_{\rm ej}^{\rm int}$ for LAMOST-HVS1. Therefore, the ejection of LAMOST-HVS1 cannot be explained by dynamical interaction of stars if all of the interacting stars are as massive as or less massive than LAMOST-HVS1.

7. Ejection Frequency

An $8\,M_\odot$ star, such as LAMOST-HVS1, can survive for $\sim$30 Myr. Thus, observable hyper-runaway stars more massive than $\sim 8\,M_\odot$ must have been ejected in the last $\sim$30 Myr or so. Currently, only one star, LAMOST-HVS1, has been confirmed (with high confidence) to be a massive hyper-runaway star with $V_{\rm ej}^{\rm int} \gtrsim 600\,\mathrm{km\,s^{-1}}$. (We note that HD 271791 is also a massive hyper-runaway star, but with $V_{\rm ej}^{\rm int} \simeq 400\,\mathrm{km\,s^{-1}}$.) Thus, we estimate that the ejection rate of massive ($\geqslant 8\,M_\odot$) hyper-runaway stars with $V_{\rm ej}^{\rm int} \gtrsim 600\,\mathrm{km\,s^{-1}}$ from the entire stellar disk of the Milky Way is at least $\sim$1 per 30 Myr.

In Section 6, we argued that the large intrinsic ejection velocity of LAMOST-HVS1 is consistent with three channels of dynamical ejection. Here, we estimate the expected number of massive hyper-runaway stars with $V_{\rm ej}^{\rm int} \gtrsim 600\,\mathrm{km\,s^{-1}}$ ejected in the last 30 Myr for these mechanisms under some optimistic but reasonable assumptions. These theoretical ejection rates would be helpful to determine whether any of the channels can naturally explain the observed ejection rate.

In Section 7.1, we explain some common assumptions. In Sections 7.2–7.4, we will discuss the theoretical ejection rates associated with (1) ordinary massive stars, (2) an IMBH, and (3) a VMS, respectively. A busy reader may skip to Section 7.5, where we summarize these ejection rates.

7.1. Assumptions on YMCs

Since all of the possible mechanisms to eject a hyper-runaway star with $M = 8\,M_\odot$ are associated with close encounter of the $8\,M_\odot$ star with more massive objects (e.g., an IMBH or VMS) and since these objects are thought to preferentially form in regions of very high stellar density (Gvaramadze et al. 2008, 2009), then we assume, as others have done, that these massive objects form rapidly in YMCs. Since these mechanisms also operate most efficiently in YMCs, then we assume them to be the sites of massive hyper-runaway ejection. In this section, we briefly summarize some of the assumptions and concepts that we use in our calculations to estimate the ejection rates.

7.1.1. Stars in YMCs

There have been extensive efforts to constrain the initial mass function (IMF) of stars in YMCs but, due to the limited range of detectable mass, it is currently difficult to determine whether their IMFs differ significantly from standard IMF models (Portegies Zwart et al. 2010). Throughout this section, we assume that the stars in a star cluster follow the Salpeter IMF (Salpeter 1955) for stellar masses in the range $0.2\,M_\odot < M < 60\,M_\odot$. Under this assumption, the mean stellar mass is $\langle M \rangle = 0.667\,M_\odot$ and each cluster contains $N_* = 1.50\,(M_{\rm cl}/M_\odot)$ stars when the cluster is formed. Star clusters with mass $M_{\rm cl} < 10^4\,M_\odot$ contain less than 10 stars with $M > 30\,M_\odot$, so we will mainly focus on massive clusters with $M_{\rm cl} \gtrsim 10^4\,M_\odot$. For a Salpeter IMF, the number of massive stars with $20\,M_\odot < M < 60\,M_\odot$ and $7\,M_\odot < M < 11\,M_\odot$ in a cluster with mass $M_{\rm cl}$ are given by

$$N^*_{(20-60)} = 2.31 \times 10^{-3}\,M_{\rm cl}/M_\odot \tag{3}$$

and

$$N^*_{(7-11)} = 5.64 \times 10^{-3}\,M_{\rm cl}/M_\odot, \tag{4}$$

respectively. In the following arguments, for simplicity, we treat each star with (20–60) $M_\odot$ as if it is a $32\,M_\odot$ star. This is justified by the fact that the mean mass for these stars is $\simeq 32\,M_\odot$. Similarly, we treat each star with (7–11) $M_\odot$ as if it is a $8\,M_\odot$ star. This is motivated by the fact that we are interested in hyper-runaway stars with $M \simeq 8\,M_\odot$.

For massive stars with $M > 7\,M_\odot$, we assume that the binary fraction is 80%. This is motivated by the observed multiplicity fraction of $\gtrsim$(60–80)% for high-mass stars (Chini et al. 2012; Duchêne & Kraus 2013). In addition, the orbital semimajor axis of each massive binary (a binary containing massive stars with $M > 7\,M_\odot$) is assumed to be $a = 30\,R_\odot$ ($\simeq$0.14 au), which roughly corresponds to the peak (but not median) of the observed distribution of a for massive binaries (see Figure 2 of Duchêne & Kraus 2013).

We assume primordial mass segregation in YMCs. This means that massive stars are already located at the core region when a YMC is formed. This kind of primordial mass segregation is discussed by Gvaramadze et al. (2009), but we note that similar mass segregation may be achieved by dynamical friction (Gvaramadze et al. 2008). In addition, motivated by numerical simulations (Portegies Zwart et al. 2010), we assume that the core radius stays small ($r_{\rm c} \simeq 0.1$ pc) for only $\sim$6 Myr. The core region then expands due to the mass loss from massive stars or supernova explosion. The timescale for core expansion is important in our calculations because the ejection rate of massive hyper-runaway stars depends on the number density of massive stars at the core. For reference, the main-sequence lifetime of 8, 30, 60 $M_\odot$ star are 30 Myr, 6 Myr, and 3 Myr, respectively (Ekström et al. 2012).

7.1.2. Cluster Mass Function

Since we are interested in the number of massive hyper-runaway stars ejected from the Milky Way in the last 30 Myr, it is important to estimate the number of YMCs (the assumed ejection sites) formed in the last 30 Myr. Following Section 2.4.2 of Portegies Zwart et al. (2010), we assume that the star

formation rate in the solar neighborhood is $\sim 5 \times 10^3\,M_\odot$ Myr $^{-1}$ kpc $^{-2}$ and that $\sim$10% of the mass is contained in bound star clusters (including YMCs) that do not expand and dissolve. Then the total mass of bound star clusters formed within $R < 10$ kpc from the Galactic Center in the last 30 Myr is $M_{\rm tot} = 4.71 \times 10^6\,M_\odot$. We assume that the mass function of star clusters formed in the last 30 Myr is given by a Schechter function with a power-law index of (−2) (Lada & Lada 2003) and scale mass of $M_{\rm Sch} = 2 \times 10^5\,M_\odot$ (Portegies Zwart et al. 2010). If the cluster mass range is $50\,M_\odot < M_{\rm cl} < 4 \times 10^5\,M_\odot$, then the mass function is given by

$$\frac{{\rm d}N_{\rm cl}}{{\rm d}\,M_{\rm cl}} = \frac{M_{\rm tot}}{7.6682}\,M_{\rm cl}^{-2}\exp\left[-\left(\frac{M_{\rm cl}}{M_{\rm Sch}}\right)\right]. \quad (5)$$

In this case, we have 546, 49 and 2 star clusters with mass of $M_{\rm cl} = (10^3$–$10^4)\,M_\odot$, $M_{\rm cl} = (10^4$–$10^5)\,M_\odot$, and $M_{\rm cl} = (10^5 - 10^{5.6})\,M_\odot$, respectively (see also Gvaramadze et al. 2008, 2009). This estimate is consistent with recent observations of YMCs more massive than $10^4\,M_\odot$. According to Table 2 and Figure 3 of Portegies Zwart et al. (2010), there are 12 YMCs that are younger than ∼20 Myr and almost all of these YMCs are distributed in the near-side of the disk. Based on the spatial distribution, we estimate that the completeness of this YMC sample with $M_{\rm cl} \gtrsim 10^4\,M_\odot$ is $f_{\rm completeness} \sim 0.25$–$0.50$. Then, the number of YMCs with $M_{\rm cl} \gtrsim 10^4\,M_\odot$ formed in the last 30 Myr is $N_{\rm cl} \sim (30\,{\rm Myr}/20\,{\rm Myr}) \times 12/f_{\rm completeness} = (36 - 72)$.

7.2. Ejection Frequency by Massive Stars with $\simeq 30\,M_\odot$

Here, we investigate the ejection frequency of early B-type main-sequence stars with $\simeq 8\,M_\odot$ by four-body interaction with more massive stars ($\sim 30\,M_\odot$; see Section 6.2.3) in the center of YMCs.

To make our calculations tractable, we specifically consider interaction between ($8\,M_\odot$, $8\,M_\odot$)- and ($32\,M_\odot$, $32\,M_\odot$)-binaries (see Section 7.1.1). In addition, we assume, for simplicity, that all binaries are equal-mass binaries. With these assumptions, as well as the assumptions in Section 7.1.1, the number of binaries in the core of a YMC with a mass $M_{\rm cl}$ can be given by $N^{\rm bin}_{(32,32)} = 0.924 \times 10^{-3}\,M_{\rm cl}/M_\odot$ for binaries with mass ($32\,M_\odot$, $32\,M_\odot$) and $N^{\rm bin}_{(8,8)} = 2.26 \times 10^{-3}\,M_{\rm cl}/M_\odot$ for binaries with mass ($8\,M_\odot$, $8\,M_\odot$).

The rate of close encounters between these binaries is given by

$$\Gamma^{\rm encounter}_{\rm bin-bin} \simeq \left(\frac{4\pi}{3}r_{\rm c}^3\right)^{-1} N^{\rm bin}_{(8,8)}\,N^{\rm bin}_{(32,32)}\,\sigma_{\rm bin-bin}\,V_{\rm rel}, \quad (6)$$

where $\sigma_{\rm bin-bin}$ is the cross section of binary–binary interaction and $V_{\rm rel}$ is the relative velocity of binaries. Unlike Leonard (1989) or Gvaramadze et al. (2008), we do not multiply by a factor 1/2 in evaluating $\Gamma^{\rm encounter}_{\rm bin-bin}$ in Equation (6), since we distinguish the two types of binaries. If we assume that only 1% of close encounters results in an ejection of a massive hyper-runaway star with $V^{\rm int}_{\rm ej} \gtrsim 600$ km s^{-1} (see Leonard 1991), we obtain the ejection rate for massive hyper-runaway stars

$$\Gamma_{\rm bin-bin} = 0.01 \times \Gamma^{\rm encounter}_{\rm bin-bin}. \quad (7)$$

We substitute $\sigma_{\rm bin-bin}$ with the cross section between a ($8\,M_\odot$, $8\,M_\odot$)- and ($32\,M_\odot$, $32\,M_\odot$)-binaries. This procedure is motivated by the simulations by Leonard (1991). We assume that the orbital semimajor axis in each binary is $a = 30\,R_\odot$. In addition, following Leonard (1989), we set the pericenter distance between these binaries to be $r_{\rm peri} = a$. These assumptions lead to a cross section of

$$\sigma_{\rm bin-bin} \simeq \frac{2\pi G\,(m_1^{\rm bin} + m_2^{\rm bin})\,a}{V_{\rm rel}^2}, \quad (8)$$

where $(m_1^{\rm bin}, m_2^{\rm bin}) = (2 \times 32\,M_\odot, 2 \times 8\,M_\odot)$ are the binary mass. Thus, the hyper-runaway ejection rate of early B-type stars due to four-body interaction with ∼4 times more massive stars in the core region of a YMC is given by

$$\Gamma_{\rm bin-bin} \simeq 1.49 \times 10^{-4}\,{\rm Myr}^{-1}\left(\frac{r_{\rm c}}{0.1\,{\rm pc}}\right)^{-3}\left(\frac{M_{\rm cl}}{10^4\,M_\odot}\right)^2 \times \left(\frac{V_{\rm rel}}{5\,{\rm km\,s^{-1}}}\right)^{-1}\left(\frac{m_1^{\rm bin} + m_2^{\rm bin}}{80\,M_\odot}\right)\left(\frac{a}{30\,R_\odot}\right). \quad (9)$$

By taking into account that this dynamical channel to eject hyper-runaway stars is active for ∼6 Myr (which is determined by the main-sequence age of $32\,M_\odot$ star[9], as well as the timescale during which the core density of a YMC is high—see Section 7.1.1), each YMC ejects ($\Gamma_{\rm bin-bin} \times 6$ Myr) massive hyper-runaway stars. To estimate the total number of massive hyper-runaway stars, we need to integrate ($\Gamma_{\rm bin-bin} \times 6$ Myr $\times\, dN_{\rm cl}/dM_{\rm cl}$) over $M_{\rm cl}$ at $10^3\,M_\odot \leqslant M_{\rm cl} \leqslant 4 \times 10^5\,M_\odot$. (The cluster mass function is given in Equation (5).) By doing this integration, we estimate that the number of massive hyper-runaway stars ejected from the stellar disk in the last 30 Myr is

$$N_{\rm bin-bin} \simeq 0.943\left(\frac{r_{\rm c}}{0.1\,{\rm pc}}\right)^{-3} \times \left(\frac{V_{\rm rel}}{5\,{\rm km\,s^{-1}}}\right)^{-1}\left(\frac{m_1^{\rm bin} + m_2^{\rm bin}}{80\,M_\odot}\right)\left(\frac{a}{30\,R_\odot}\right). \quad (10)$$

Here, we implicitly assume that the core radius r_c is common for all YMCs. Since $\Gamma_{\rm bin\text{-}bin}$ scales as $M_{\rm cl}^2$, a small number of very massive YMCs have some impact on $N_{\rm bin\text{-}bin}$. For example, if the integration range is $10^4\,M_\odot \leqslant M_{\rm cl} \leqslant 4 \times 10^5\,M_\odot$ and $10^5\,M_\odot \leqslant M_{\rm cl} \leqslant 4 \times 10^5\,M_\odot$, then the representative number of hyper-runaway ejections (which is 0.943 in Equation (10)) are $N_{\rm bin\text{-}bin} \simeq 0.895$ and 0.517, respectively. This is remarkable given that we expect only ≃2 YMCs more massive than $10^5\,M_\odot$ in the last 30 Myr (see Section 7.1.2). This also means that our estimation on $N_{\rm bin\text{-}bin}$ will be affected by Poisson fluctuations on the number of very massive YMCs. In any case, our simple analysis suggests that the ejection of LAMOST-HVS1, an $8\,M_\odot$ massive hyper-runaway star with $V^{\rm int}_{\rm ej} \sim 600$ km s^{-1}, can be

[9] For more massive stars, the main-sequence age is shorter. However, they have larger mass and larger cross-section, so it does not affect our estimation. This is another justification for treating massive stars with $M = (20$–$60)\,M_\odot$ as if they are $32\,M_\odot$ stars.

marginally explained if we consider binary–binary interaction at the high-density core region of YMCs.

7.3. Ejection Frequency by an IMBH

If a YMC harbors an IMBH, then it can eject massive hyper-runaway stars through the Hills mechanism (Hills 1988; Yu & Tremaine 2003; Bromley et al. 2006; Gvaramadze et al. 2008; Brown 2015). When a binary system with the semimajor axis a consisting of stars with mass (m_1, m_2) approaches near the tidal breakup radius of

$$r_t = \left(\frac{3M_{\rm BH}}{m_1+m_2}\right)^{1/3} a, \tag{11}$$

the binary is disrupted with some probability. If one of the stars, say the primary star (m_1), is captured by the IMBH, then the secondary star (m_2) is ejected with a large velocity due to the energy conservation. Numerical experiments (e.g., Bromley et al. 2006) suggest that the intrinsic ejection velocity of a star with mass m_2 is given by

$$V_{\rm ej}^{\rm int} \simeq 521\ {\rm km\ s^{-1}} \left(\frac{M_{\rm BH}}{100\,M_\odot}\right)^{1/6} \left(\frac{30\,R_\odot}{a}\right)^{1/2} \times \left(\frac{m_1+m_2}{16\,M_\odot}\right)^{1/3} \left(\frac{2m_1}{m_1+m_2}\right)^{1/2} f_R. \tag{12}$$

Here, $f_R(D) \leqslant 1$ is an empirical factor of order unity that depends on a dimensionless variable

$$D = \frac{r_{\rm peri}}{a}\left(\frac{10^6\,M_\odot}{M_{\rm BH}}\frac{(m_1+m_2)}{2\,M_\odot}\right)^{1/3}, \tag{13}$$

where $r_{\rm peri}$ is the pericentric distance of the orbit of the binary with respect to the IMBH (Hills 1988). The function $f_R(D)$ shows a non-monotonic, unimodal shape. Its shape can be inferred from Figure 3 of Hills (1988). The approximate expression for f_R is given by

$$f_R(D) = \sum_{k=0}^{5} c_k D^k \ (\text{for } 0 \leqslant D \leqslant 175) \tag{14}$$

with $(c_0, c_1, c_2, c_3, c_4, c_5) = (0.774,\ 0.0204,\ -6.23\times10^{-4},\ 7.62\times10^{-6},\ -4.24\times10^{-8},\ 8.62\times10^{-11})$ (Bromley et al. 2006). The factor D is also related to the empirical ejection probability of

$$P_{\rm ej} = \begin{cases} 1 - D/175 & (\text{for } 0 \leqslant D \leqslant 175), \\ 0 & (\text{for } 175 < D) \end{cases} \tag{15}$$

(see Figure 1 of Hills 1988).

Let us consider the rate of hyper-runaway ejection with $V_{\rm ej}^{\rm int} \geqslant 600\,{\rm km\ s^{-1}}$ of a star with $m_2 = 8\,M_\odot$. Equation (12) implies that $V_{\rm ej}^{\rm int}$ is smaller for larger a. Given Equation (12) and the fact that $f_R \leqslant 1$, the condition of $V_{\rm ej}^{\rm int} \geqslant 600\,{\rm km\ s^{-1}}$ imposes a necessary condition

$$a \leqslant a_{\rm crit} \equiv 22.6\,R_\odot \left(\frac{M_{\rm BH}}{10^2\,M_\odot}\right)^{1/3} \times \left(\frac{m_1+m_2}{16\,M_\odot}\right)^{2/3} \left(\frac{2m_1}{m_1+m_2}\right). \tag{16}$$

If $a \leqslant a_{\rm crit}$ is satisfied, then there exists a certain range of D and therefore $r_{\rm peri}$ such that $V_{\rm ej}^{\rm int} \geqslant 600\,{\rm km\ s^{-1}}$. For a given $(M_{\rm BH}, m_1, m_2, a)$, the allowed range of $r_{\rm peri}$ for hyper-runaway ejection can be numerically evaluated by using Equation (14). Due to the unimodal shape of f_R, the allowed range of $r_{\rm peri}$ can be expressed as[10]

$$r_{\rm peri,min} \leqslant r_{\rm peri} \leqslant r_{\rm peri,max}. \tag{17}$$

Roughly speaking, the value of $r_{\rm peri,max}$ can be regarded as the maximum impact parameter for hyper-runaway ejection. Since $f_R(D)$ is a non-monotonic function, smaller D (or smaller impact parameter) does not necessarily result in larger ejection velocity (see Figure 3 of Hills 1988). Thus, $r_{\rm peri,min}$ can have a non-zero value. The effective cross section for interaction between the binaries with mass (m_1, m_2) and the IMBH that results in a hyper-runaway ejection is given by

$$\sigma_{\rm BH-bin} \simeq \frac{2\pi G(M_{\rm BH}+m_1+m_2) r_{\rm peri,max} f_{\rm corr}}{V_{\rm rel}^2}. \tag{18}$$

Here, $0 \leqslant f_{\rm corr} \leqslant 1$ is a correction factor given by

$$f_{\rm corr} = \frac{1}{r_{\rm peri,max}} \int_{r_{\rm peri,min}}^{r_{\rm peri,max}} {\rm d}r\ P_{\rm ej} \tag{19}$$

that takes into account the ejection probability as a function of $r_{\rm peri}$ (see Equation (15)). (If $P_{\rm ej} = 1$ and $r_{\rm peri,min} = 0$, we have $f_{\rm corr} = 1$ and thus Equation (18) looks similar to Equation (8).) The collision rate between a given IMBH and the surrounding binaries is

$$\Gamma_{\text{each-IMBH}} = \left(\frac{4\pi}{3}r_{\rm c}^3\right)^{-1} N^{\rm bin}\sigma_{\rm BH-bin}V_{\rm rel}, \tag{20}$$

where $N^{\rm bin}$ is the number of the binaries near the IMBH.

Now let us evaluate $\Gamma_{\rm each-IMBH}$ for representative environments. Here, we fix $m_2 = 8\,M_\odot$, $a = 30\,R_\odot$, and $V_{\rm rel} = 5$ km s^{-1}. We assume that the core radii of YMCs are identical. We also assume that those YMCs with $M_{\rm cl} > 10^4\,M_\odot$ harbor a $10^2\,M_\odot$ IMBH, and those with $M_{\rm cl} > 10^5\,M_\odot$ harbor a $10^3\,M_\odot$ IMBH.

(Case 1)—If $(M_{\rm BH}, m_1) = (10^2\,M_\odot, 8\,M_\odot)$, the hyper-runaway ejection does not happen because $a = 30\,R_\odot \not\leqslant a_{\rm crit} = 22.6\,R_\odot$.

(Case 2)—If $(M_{\rm BH}, m_1) = (10^2\,M_\odot, 32\,M_\odot)$, the allowed range of $r_{\rm peri}$ (see Equation (17)) is $0 \leqslant r_{\rm peri} \leqslant 72.3\,R_\odot$ and $f_{\rm corr} = 0.597$. We assume that the number of stars with $32\,M_\odot$ is given by N^*_{20-60} and assume the binary fraction of 80%. For simplicity, we also assume that the binary companion of a $32\,M_\odot$ star is always a $8\,M_\odot$ star. The number of binaries with mass (m_1, m_2) in the core of a YMC is given by

[10] If a is exactly equal to $a_{\rm crit}$ or slightly smaller than it, then the allowed range of $r_{\rm peri}$ is very narrow, which results in very low probability of hyper-runaway ejection.

$N^{\rm bin} = 0.8 \times N^{*}_{20-60} = 1.85 \times 10^{-3}(M_{\rm cl}/M_{\odot})$. In this case, we obtain

$$\Gamma^{(2)}_{\text{each-IMBH}} \simeq 3.32 \times 10^{-3}\,\text{Myr}^{-1}\left(\frac{r_{\rm c}}{0.1\,\text{pc}}\right)^{-3}\left(\frac{M_{\rm cl}}{10^4\,M_{\odot}}\right) \times \left(\frac{V_{\rm rel}}{5\,\text{km s}^{-1}}\right)^{-1}. \quad (21)$$

Since the main-sequence lifetime of a $32\,M_{\odot}$ star is $\sim$6 Myr, a $100\,M_{\odot}$ IMBH in a YMC ejects $N^{(2)}_{\text{each-IMBH}} = (\Gamma^{(2)}_{\text{each-IMBH}} \times 6$ Myr) massive hyper-runaway stars during this 6 Myr period. If YMCs have an identical core radius r_c, then the total number of massive hyper-runaway stars from the stellar disk is proportional to the total mass of the YMCs that harbor an IMBH. Given that 31.5% of $M_{\rm tot}$ is embedded in YMCs with $M_{\rm cl} > 10^4\,M_{\odot}$ in our cluster mass function in Equation (5), we estimate that

$$N^{(2)}_{\text{all-IMBH}} \sim 2.96\left(\frac{r_{\rm c}}{0.1\,\text{pc}}\right)^{-3}\left(\frac{V_{\rm rel}}{5\,\text{km s}^{-1}}\right)^{-1} \quad (22)$$

massive hyper-runaway stars are ejected from the stellar disk in the last 30 Myr.

(Case 3)—If $(M_{\rm BH}, m_1) = (10^3\,M_{\odot}, 8\,M_{\odot})$, then the allowed range of $r_{\rm peri}$ is $0.84\,R_{\odot} \leqslant r_{\rm peri} \leqslant 174\,R_{\odot}$ and $f_{\rm corr} = 0.664$. We assume that the number of stars with $\sim 8\,M_{\odot}$ is given by N^{*}_{7-11} and that the binary fraction is 80%. For simplicity, we also assume that these binaries are equal-mass binaries. The number of binaries with mass $(8\,M_{\odot}, 8\,M_{\odot})$ in the core of a YMC is given by $N^{\rm bin} = 0.8 \times 0.5 \times N^{*}_{7-11} = 2.26 \times 10^{-3}(M_{\rm cl}/M_{\odot})$. In this case, we obtain

$$\Gamma^{(3)}_{\text{each-IMBH}} \simeq 7.86 \times 10^{-2}\,\text{Myr}^{-1}\left(\frac{r_{\rm c}}{0.1\,\text{pc}}\right)^{-3}\left(\frac{M_{\rm cl}}{10^4\,M_{\odot}}\right) \times \left(\frac{V_{\rm rel}}{5\,\text{km s}^{-1}}\right)^{-1} \quad (23)$$

Although the main-sequence age of an $8\,M_{\odot}$ star is $\sim$30 Myr, we assume that this ejection can last for 6 Myr, by taking into account that the core of YMCs begin to expand and the density decreases in the early phase of YMC formation (Portegies Zwart et al. 2010). Then, a $10^3\,M_{\odot}$ IMBH in a YMC ejects $N^{(3)}_{\text{each-IMBH}} = (\Gamma^{(3)}_{\text{each-IMBH}} \times 10$ Myr) massive hyper-runaway stars during this 6 Myr period. By assuming that those clusters with $M_{\rm cl} > 10^5\,M_{\odot}$ (that weigh 6.66% of $M_{\rm tot}$) harbor a $10^3\,M_{\odot}$ IMBH, we estimate that

$$N^{(3)}_{\text{all-IMBH}} \sim 14.8\left(\frac{r_{\rm c}}{0.1\,\text{pc}}\right)^{-3}\left(\frac{V_{\rm rel}}{5\,\text{km s}^{-1}}\right)^{-1} \quad (24)$$

massive hyper-runaway stars are ejected from the stellar disk in the last 30 Myr.

(Case 4)—If $(M_{\rm BH}, m_1) = (10^3\,M_{\odot}, 32\,M_{\odot})$, then $0 \leqslant r_{\rm peri} \leqslant 193.4\,R_{\odot}$ is allowed and $f_{\rm corr} = 0.500$. As in Case 2, we adopt a value of $N^{\rm bin} = 0.8 \times N^{*}_{20-60} = 1.85 \times 10^{-3}(M_{\rm cl}/M_{\odot})$. In this case, we obtain

$$\Gamma^{(4)}_{\text{each-IMBH}} \simeq 5.51 \times 10^{-2}\,\text{Myr}^{-1}\left(\frac{r_{\rm c}}{0.1\,\text{pc}}\right)^{-3}\left(\frac{M_{\rm cl}}{10^4\,M_{\odot}}\right) \times \left(\frac{V_{\rm rel}}{5\,\text{km s}^{-1}}\right)^{-1}. \quad (25)$$

Since the main-sequence lifetime of a $32\,M_{\odot}$ star is $\sim$6 Myr, a $10^3\,M_{\odot}$ IMBH in a YMC ejects $N^{(4)}_{\text{each-IMBH}} = (\Gamma^{(4)}_{\text{each-IMBH}} \times 6$ Myr) massive hyper-runaway stars during this 6 Myr period. As in Case 2, we estimate that

$$N^{(4)}_{\text{all-IMBH}} \sim 10.4\left(\frac{r_{\rm c}}{0.1\,\text{pc}}\right)^{-3}\left(\frac{V_{\rm rel}}{5\,\text{km s}^{-1}}\right)^{-1} \quad (26)$$

massive hyper-runaway stars are ejected from the stellar disk in the last 30 Myr.

7.4. Ejection Frequency by a VMS

If a YMC harbors a VMS, then it can eject massive hyper-runaway stars through the Hills mechanism—just as an IMBH does. Here, we explain two differences between the hyper-runaway ejection by an IMBH and that by a VMS.

First, in the VMS ejection, the stellar binary has to have $r_{\rm peri}$ that is larger than the radius of the VMS, $R_{\rm VMS}$; otherwise, the binary may merge with the VMS (Gvaramadze et al. 2009). In the following discussion, we assume that a $100\,M_{\odot}$ star has an radius of $18\,R_{\odot}$ (Ishii et al. 1999). We note that VMSs with $M \gtrsim 133\,M_{\odot}$ (Ishii et al. 1999; Yungelson et al. 2008) are predicted to show a core-halo configuration (Kato 1985) such that the mass contribution from the stellar outer diffuse layer is negligible. Following Gvaramadze et al. (2009), we assume that the mass of a $10^3\,M_{\odot}$ VMS is effectively contained within a radius of $40\,R_{\odot}$.

Second, a VMS, unlike an IMBH, is not expected to survive for a long time. The finite age of a VMS determines the duration of time when a VMS ejects hyper-runaway stars. When a VMS forms through continuous mergers of massive stars, it can survive longer—due to the rejuvenation—than an isolated main-sequence star with the same mass. Since the detailed modeling of VMSs is still not satisfactory due to the uncertainty in the mass loss rate of VMSs (Vink 2015) and in the rejuvenation process (Schneider et al. 2016), in the following we simply assume that the lifetime of a VMS of any mass is 5 Myr, motivated by the results in Portegies Zwart et al. (1999). For simplicity, we also assume that a VMS is formed instantaneously just after the formation of a YMC and its mass is constant as a function of time. This assumption means that in our toy VMS model, the stellar mass loss is compensated by the growth of the mass as a result of mergers.

In the following, we consider Cases 2, 3, and 4 as in Section 7.3. We do not consider Case 1 because it obviously results in no massive hyper-runaway stars. In addition to the above-mentioned assumptions, we assume that those YMCs with $M_{\rm cl} > 10^4\,M_{\odot}$ harbor a $10^2\,M_{\odot}$ VMS, and those with $M_{\rm cl} > 10^5\,M_{\odot}$ harbor a $10^3\,M_{\odot}$ VMS, as in Section 7.3.

(Case 2)—If $(M_{\rm VMS}, m_1) = (10^2\,M_{\odot}, 32\,M_{\odot})$, the allowed range of $r_{\rm peri}$ is altered to $(R_{\rm VMS} =)18\,R_{\odot} \leqslant r_{\rm peri} \leqslant 72.3\,R_{\odot}$ and we have $f_{\rm corr} = 0.373$. We obtain $\Gamma^{(2)}_{\text{each-VMS}} = 0.625\Gamma^{(2)}_{\text{each-IMBH}}$. If we assume that a $10^2\,M_{\odot}$ VMS in a YMC survives for 5 Myr,

then it ejects $N^{(2)}_{\text{each-VMS}} = 0.521 N^{(2)}_{\text{each-IMBH}}$ massive hyper-runaway stars during this period. By repeating the same arguments as in Section 7.3, we estimate that

$$N^{(2)}_{\text{all-VMS}} \sim 1.54 \left(\frac{r_c}{0.1\ \text{pc}}\right)^{-3} \left(\frac{V_{\text{rel}}}{5\ \text{km s}^{-1}}\right)^{-1} \quad (27)$$

massive hyper-runaway stars are ejected from the stellar disk in the last 30 Myr.

(Case 3)—If $(M_{\text{VMS}}, m_1) = (10^3\,M_\odot, 8\,M_\odot)$, the allowed range of r_{peri} is altered to $(R_{\text{VMS}} =)40\,R_\odot \leqslant r_{\text{peri}} \leqslant 174.0\,R_\odot$ and we have $f_{\text{corr}} = 0.456$. We obtain $\Gamma^{(3)}_{\text{each-VMS}} = 0.687\Gamma^{(3)}_{\text{each-IMBH}}$. If we assume that a $10^3\,M_\odot$ VMS in a YMC survives for 5 Myr, then it ejects $N^{(3)}_{\text{each-VMS}} = 0.573 N^{(3)}_{\text{each-IMBH}}$ massive hyper-runaway stars during this period. By repeating the same arguments, we estimate that

$$N^{(3)}_{\text{all-VMS}} \sim 8.48 \left(\frac{r_c}{0.1\ \text{pc}}\right)^{-3} \left(\frac{V_{\text{rel}}}{5\ \text{km s}^{-1}}\right)^{-1} \quad (28)$$

massive hyper-runaway stars are ejected from the stellar disk in the last 30 Myr.

(Case 4)—If $(M_{\text{VMS}}, m_1) = (10^3\,M_\odot, 32\,M_\odot)$, the allowed range of r_{peri} is altered to $(R_{\text{VMS}} =)40\,R_\odot \leqslant r_{\text{peri}} \leqslant 193.4\,R_\odot$ and we have $f_{\text{corr}} = 0.315$. We obtain $\Gamma^{(4)}_{\text{each-VMS}} = 0.629\Gamma^{(4)}_{\text{each-IMBH}}$. If we assume that a $10^3\,M_\odot$ VMS in a YMC survives for 5 Myr, then it ejects $N^{(4)}_{\text{each-VMS}} = 0.524 N^{(4)}_{\text{each-IMBH}}$ massive hyper-runaway stars during this period. By repeating the same arguments, we estimate that

$$N^{(4)}_{\text{all-VMS}} \sim 5.45 \left(\frac{r_c}{0.1\ \text{pc}}\right)^{-3} \left(\frac{V_{\text{rel}}}{5\ \text{km s}^{-1}}\right)^{-1} \quad (29)$$

massive hyper-runaway stars are ejected from the stellar disk in the last 30 Myr.

7.5. Summary and Discussion on the Massive Hyper-runaway Star Ejection Frequency

In Sections 7.2–7.4, we explored the ejection frequency of massive ($\gtrsim 8\,M_\odot$) hyper-runaway stars with $V^{\text{int}}_{\text{ej}} \gtrsim 600\ \text{km s}^{-1}$ (comparable to the ejection velocity of LAMOST-HVS1). Since the ejection rate is proportional to the number density of massive binaries (for IMBH and VMS ejection) or the number density squared (for binary–binary interaction), massive hyper-runaway ejection requires a high density. Furthermore, since all of these mechanisms are involved with massive objects, hyper-runaway ejection must occur in young star-forming regions. These requirements seem to indicate that massive hyper-runaway ejection only happens in YMCs.

We estimate that the number of massive hyper-runaway stars ejected in the last 30 Myr from the stellar disk of the Milky Way is ∼1 for binary–binary encounter of ordinary stars; ∼(3–15) for ejection by an IMBH; and ∼(2–8) for ejection by a VMS. Since LAMOST-HVS1 is the only well-confirmed example of a massive hyper-runaway star with $V^{\text{int}}_{\text{ej}} \gtrsim 600\ \text{km s}^{-1}$ that was ejected in the last ∼30 Myr, it is interesting that all of the above-mentioned dynamical channels can explain the ejection of LAMOST-HVS1. However, we should bear in mind that we have made some simplistic assumptions in estimating the ejection frequency. For example, we can easily change the ejection frequency by a factor of a few with some fine-tuning of the parameters used. Some obvious sources of uncertainties include the influence from the adopted IMF (Section 7.1.1) and the mass function of the YMCs (Section 7.1.2).

Although the absolute value of our ejection frequency may not be very accurate, our results are still useful in understanding the relative efficiency in ejecting hyper-runaway stars. Here we compare the ejection by an IMBH and VMS. Our results suggest that a $100\,M_\odot$ IMBH is ∼2 times more efficient in ejecting hyper-runaway stars than a $100\,M_\odot$ VMS. This difference arises from the fact that a very close encounter with an IMBH may result in a hyper-runaway star, while a very close encounter with a VMS will end up with a merger instead. Of course, this result alone does not favor IMBH-origin over VMS-origin, since forming a $100\,M_\odot$ IMBH is probably more difficult than forming a VMS with the same mass. Also, we note that no IMBH has been detected in YMCs in the Milky Way, while some massive stars in YMCs are regarded as remnants of VMSs.

Our estimate of the ejection frequency by binary–binary interactions is smaller than those by an IMBH or a VMS. However, we regard this ejection channel to be promising because it requires multiple ordinary massive stars ($\sim 30\,M_\odot$) and it does not require any exotic objects or phenomena. Our simple estimate suggests that the ejection of massive hyper-runaway star with $V^{\text{int}}_{\text{ej}} \gtrsim 600\ \text{km s}^{-1}$ can occur every ∼30 Myr. Since the ejection frequency in this scenario is proportional to the square of the number density of massive binaries (see Equations (6) and (7)), the ejection rate can be enhanced by a factor of X^2 if the number density of massive objects is increased by a factor of X by adopting a top-heavy IMF. In addition, since the ejection frequency from a given YMC is proportional to M^2_{cl} (see Equation (9)), the total number of hyper-runaway stars is increased if a larger number of very massive YMCs have been formed in the last 30 Myr. Such an overproduction of very massive YMCs can happen as a result of Poisson fluctuations. Indeed, under our assumption of the cluster mass function, the number of massive clusters with mass $10^5\,M_\odot < M_{\text{cl}} < 10^{5.6}\,M_\odot$ formed in the last 30 Myr is expected to be two (Section 7.1.2), so the Poisson fluctuation may result in 70% $(=\sqrt{2}/2)$ overproduction or underproduction of YMCs with $10^5\,M_\odot < M_{\text{cl}} < 10^{5.6}\,M_\odot$. This results in 40% $(=(\sqrt{2}/2) \times 0.517/0.943)$ overproduction or underproduction of massive hyper-runaway stars. In any case, our calculations encourage more detailed simulations of four-body interaction of ordinary massive stars in YMCs dedicated to study massive hyper-runaway stars (Leonard 1991; Fujii & Portegies Zwart 2011; Perets & Šubr 2012).

If our estimate of the ejection frequency is correct to a factor of a few, then IMBHs or VMSs in the Milky Way may have ejected at least a few more massive hyper-runaway stars with $V^{\text{int}}_{\text{ej}} \gtrsim 600\ \text{km s}^{-1}$. There is also some room for the four-body interaction of ordinary massive stars to have ejected a few more massive hyper-runaway stars. If more massive hyper-runaway stars are discovered or confirmed in the future, then this will further motivate us to study the ejection mechanism of massive hyper-runaway stars.

8. Discussion and Conclusion

We obtained high-resolution spectra of LAMOST-HVS1 with MIKE spectrograph mounted on *Magellan* Telescope and confirmed that this star is an $8.3\,M_\odot$ B-type subgiant star with super-solar metallicity ($[\text{Si/H}] = 0.60 \pm 0.06$, $[\text{Mg/H}] = 0.33 \pm 0.10$; Table 2). We have been able to reconstruct the

orbit of this star by using the proper motion from *Gaia* DR2, the spectroscopic distance and the line-of-sight velocity (Table 1). The orbital analysis suggests that this star was ejected from the inner stellar disk of the Milky Way ($R_{\rm ej} = 2.9^{+2.5}_{-0.9}$ kpc) with the intrinsic ejection velocity (corrected for the disk streaming motion) $V_{\rm ej}^{\rm int} = 568^{+19}_{-17}$ km s^{-1} (Figures 3 and 5). The ejection happened $\sim$33 Myr ago, probably just after the formation of this star in the natal star cluster. The chemical abundance pattern of LAMOST-HVS1 is similar to that of inner-disk young massive stars (see Table 2 and Section 5.7), which supports the disk origin of this star.

The large intrinsic ejection velocity of LAMOST-HVS1 rules out the possibility that this star was ejected by the supernova explosion of the binary companion. Rather, this star was probably ejected by a few-body dynamical interaction with more massive objects in a high-density environment. Such an extreme environment may be attained in the core region of a YMC with mass of $\gtrsim 10^4\,M_\odot$.

Based on the flight time and the ejection location of LAMOST-HVS1, we argue that its ejection agent (the other object that took part in this ejection) or the natal star cluster must be currently located in the inner disk, probably near the Norma spiral arm (Figure 7). If the natal star cluster of LAMOST-HVS1 is as massive as $\sim 10^4\,M_\odot$, then we expect that the cluster survives until today. The current locations and ages of the known YMCs, as well as the estimated current location of the natal star cluster of LAMOST-HVS1 indicate that none of the known YMCs can be the natal cluster of LAMOST-HVS1 and, therefore, it may imply the existence of an undiscovered YMC.

LAMOST-HVS1 is the first well-confirmed early B-type massive ($\gtrsim 8\,M_\odot$) hyper-runaway star with $V_{\rm ej}^{\rm int} \gtrsim 600$ km s^{-1} ejected from the inner Galactic disk. This fact suggests that the ejection frequency of such massive hyper-runaway stars from the entire stellar disk of the Milky Way is $\gtrsim$1 per 30 Myr. We argue that this rough estimate of the ejection frequency can be explained by a few-body interaction associated with either an IMBH ($\gtrsim 100\,M_\odot$), a VMS ($\gtrsim 100\,M_\odot$), or multiple ordinary massive stars ($\gtrsim 30\,M_\odot$) (Sections 6 and 7). If more massive hyper-runaway stars are discovered in the future, then this will help us to understand the origin of massive hyper-runaway stars and the dynamics of the extreme environment in which massive stars form.

We thank the members of the stellar halos group at the University of Michigan for their stimulating discussion. We thank Mark Reynolds for discussion on Galactic X-ray sources. We thank Mark Gieles for providing us with the coordinate information of YMCs. We thank the staff and workers at the 6.5 m *Magellan* Telescopes at the Las Campanas Observatory, Chile, for their labor. M.V. and K.H. are supported by NASA-ATP award NNX15AK79G. I.U.R. acknowledges support from grants PHY 14-30152 (Physics Frontier Center/JINA-CEE), AST 16-13536, and AST 18-15403 awarded by the U.S. National Science Foundation (NSF). This research was started at the NYC *Gaia* DR2 Workshop at the Center for Computational Astrophysics of the Flatiron Institute in 2018 April. This work has made use of data from the European Space Agency (ESA) mission *Gaia* (http://www.cosmos.esa.int/gaia), processed by the *Gaia* Data Processing and Analysis Consortium (DPAC, http://www.cosmos.esa.int/web/gaia/dpac/consortium). Funding for the DPAC has been provided by national institutions, in particular the institutions participating in the *Gaia* Multilateral Agreement. Guoshoujing Telescope (the Large Sky Area Multi-Object Fiber Spectroscopic Telescope LAMOST) is a National Major Scientific Project built by the Chinese Academy of Sciences. Funding for the project has been provided by the National Development and Reform Commission. LAMOST is operated and managed by the National Astronomical Observatories, Chinese Academy of Sciences. This research has made use of NASA's Astrophysics Data System Bibliographic Services; the arXiv pre-print server operated by Cornell University; the SIMBAD and VizieR databases hosted by the Strasbourg Astronomical Data Center.

Facilities: *Gaia*, *Magellan*.

Software: Agama (Vasiliev 2019), corner.py (Foreman-Mackey 2016), matplotlib (Hunter 2007), numpy (van der Walt et al. 2011), scipy (Jones et al. 2001).

Appendix
A Note on the Quality of the Astrometric Solution

We need to be careful about the quality of the astrometric solution when using the *Gaia* data. To assess whether or not the astrometric data for LAMOST-HVS1 are reliable, we checked some statistical indicators in *Gaia* DR2 for this star.

First, we checked the criteria (i)–(iv) in Section 4 of Marchetti et al. (2018), which are based on the *Gaia* documentation as of 2018 April (when *Gaia* DR2 was released):

(i) ASTROMETRIC_GOF_AL < 3;
(ii) ASTROMETRIC_EXCESS_NOISE_SIG $\leqslant 2$;
(iii) $-0.23 \leqslant$ MEAN_VARPI_FACTOR_AL $\leqslant 0.32$;
(iv) VISIBILITY_PERIODS_USED > 8.

For LAMOST-HVS1, we have ASTROMETRIC_GOF_AL $= 22.03$, ASTROMETRIC_EXCESS_NOISE_SIG $= 32.46$, MEAN_VARPI_FACTOR_AL $= -0.06760$, and VISIBILITY_PERIODS_USED $= 9$; therefore the criteria (i) and (ii) are not satisfied but (iii) and (iv) are satisfied.

Second, we checked the distributions of (i) ASTROMETRIC_GOF_AL and (ii) ASTROMETRIC_EXCESS_NOISE_SIG for those stars for which the G magnitude is similar to that of LAMOST-HVS1. Given that the reported parallax for LAMOST-HVS1 is negative, we checked the distributions of these quantities for stars with positive parallax and negative parallax. Consequently, we found that both ASTROMETRIC_GOF_AL and ASTROMETRIC_EXCESS_NOISE_SIG are typically much larger than the *Gaia*'s recommended upper limits (3 and 2, respectively) when the parallax is negative. This indicates that the large values of ASTROMETRIC_GOF_AL and ASTROMETRIC_EXCESS_NOISE_SIG for LAMOST-HVS1 may be related to the negative parallax of this star. (It is not surprising that the goodness-of-fit of an astrometric solution is poor if the reported parallax is negative.)

Lastly, we checked the quality flag that was more recently proposed. According to Lindegren (2018) (*Gaia* DPAC document published in August 2018), a quantity called "renormalized unit weight error" (RUWE) may be a better way of assessing the quality of the astrometric solution. Here,

RUWE is given by

$$\mathrm{RUWE} = \frac{1}{u_0(G,\, G_{\mathrm{BP}} - G_{\mathrm{RP}})} \times \sqrt{\frac{\mathrm{ASTROMETRIC\_CHI2\_AL}}{\mathrm{ASTROMETRIC\_N\_GOOD\_OBS\_AL} - 5}}, \quad (30)$$

and u_0 is a normalization factor. From the available data of ASTROMETRIC_CHI2_AL = 916.65, ASTROMETRIC_N_GOOD_OBS_AL = 141, $G = 13.06$, $(G_{\mathrm{BP}} - G_{\mathrm{RP}}) = -0.2316$, and $u_0(G,\ G_{\mathrm{BP}} - G_{\mathrm{RP}}) = 2.11399$ for this star,[11] we obtain RUWE = 1.228. The value of RUWE is close to 1.0 and smaller than 1.4, which is expected for a well-behaved astrometric solution (Lindegren 2018). Thus, the astrometric solution for LAMOST-HVS1 is probably well-behaved given its magnitude and color.

Based on these assessments (especially the assessment of RUWE), we think that the use of *Gaia* proper motion for this star is justified. The rather large values of the above-mentioned flags (i) and (ii) are probably related to the negative parallax, but we note that the *Gaia* parallax is not used in our analysis. We will revisit the orbital analysis of LAMOST-HVS1 with future data releases, for which the astrometric data are expected to be improved.

ORCID iDs

Kohei Hattori https://orcid.org/0000-0001-6924-8862
Monica Valluri https://orcid.org/0000-0002-6257-2341
Ian U. Roederer https://orcid.org/0000-0001-5107-8930
Guillaume Mahler https://orcid.org/0000-0003-3266-2001
Gourav Khullar https://orcid.org/0000-0002-3475-7648

References

Aarseth, S. J., & Hills, J. G. 1972, A&A, 21, 255
Aerts, C., Simón-Díaz, S., Groot, P. J., & Degroote, P. 2014, A&A, 569, A118
Asplund, M., Grevesse, N., Sauval, A. J., & Scott, P. 2009, ARA&A, 47, 481
Behr, B. B. 2003, ApJS, 149, 67
Behr, B. B., Cohen, J. G., & McCarthy, J. K. 2000, ApJL, 531, L37
Behr, B. B., Cohen, J. G., McCarthy, J. K., & Djorgovski, S. G. 1999, ApJL, 517, L135
Bernstein, R., Shectman, S. A., Gunnels, S. M., Mochnacki, S., & Athey, A. E. 2003, Proc. SPIE, 4841, 1694
Blaauw, A. 1961, BAN, 15, 265
Blaauw, A. 1993, in ASP Conf. Ser. 35, Massive Stars: Their Lives in the Interstellar Medium, ed. J. P. Cassinelli & E. B. Churchwell (San Francisco, CA: ASP), 207
Bonanos, A. Z., López-Morales, M., Hunter, I., & Ryans, R. S. I. 2008, ApJL, 675, L77
Boubert, D., Fraser, M., Evans, N. W., Green, D. A., & Izzard, R. G. 2017, A&A, 606, A14
Bovy, J. 2015, ApJS, 216, 29
Bovy, J. 2017, MNRAS, 470, 1360
Bromley, B. C., Kenyon, S. J., Geller, M. J., et al. 2006, ApJ, 653, 1194
Brown, W. R. 2015, ARA&A, 53, 15
Brown, W. R., Geller, M. J., & Kenyon, S. J. 2014, ApJ, 787, 89
Brown, W. R., Lattanzi, M. G., Kenyon, S. J., & Geller, M. J. 2018, ApJ, 866, 39
Cardelli, J. A., Clayton, G. C., & Mathis, J. S. 1989, ApJ, 345, 245
Carigi, L., Peimbert, M., Esteban, C., & García-Rojas, J. 2005, ApJ, 623, 213
Castro, N., Urbaneja, M. A., Herrero, A., et al. 2012, A&A, 542, A79
Cescutti, G., Matteucci, F., François, P., & Chiappini, C. 2007, A&A, 462, 943
Chini, R., Hoffmeister, V. H., Nasseri, A., Stahl, O., & Zinnecker, H. 2012, MNRAS, 424, 1925
Conlon, E. S., Dufton, P. L., Keenan, F. P., & Leonard, P. J. T. 1990, A&A, 236, 357
Cutri, R. M., Skrutskie, M. F., van Dyk, S., et al. 2003, yCat, 2246
Davies, B., Origlia, L., Kudritzki, R.-P., et al. 2009, ApJ, 696, 2014
de Wit, W. J., Testi, L., Palla, F., & Zinnecker, H. 2005, A&A, 437, 247
Dorman, B., Rood, R. T., & O'Connell, R. W. 1993, ApJ, 419, 596
Duchêne, G., & Kraus, A. 2013, ARA&A, 51, 269
Edelmann, H., Napiwotzki, R., Heber, U., Christlieb, N., & Reimers, D. 2005, ApJL, 634, L181
Ekström, S., Georgy, C., Eggenberger, P., et al. 2012, A&A, 537, A146
Erkal, D., Boubert, D., Gualandris, A., Evans, N. W., & Antonini, F. 2019, MNRAS, 483, 2007
Esteban, C., García-Rojas, J., Peimbert, M., et al. 2005, ApJL, 618, L95
Fabbian, D., Recio-Blanco, A., Gratton, R. G., & Piotto, G. 2005, A&A, 434, 235
Figer, D. F., Najarro, F., Morris, M., et al. 1998, ApJ, 506, 384
Foreman-Mackey, D. 2016, JOSS, 1, 24
Fornasini, F. M., Tomsick, J. A., Hong, J., et al. 2017, ApJS, 229, 33
Fragione, G., & Gualandris, A. 2018, arXiv:1808.07878
Freeman, K., & Bland-Hawthorn, J. 2002, ARA&A, 40, 487
Fujii, M. S., & Portegies Zwart, S. 2011, Sci, 334, 1380
Gaia Collaboration, Brown, A. G. A., Vallenari, A., et al. 2018, A&A, 616, A1
Gies, D. R., & Bolton, C. T. 1986, ApJS, 61, 419
Glaspey, J. W., Michaud, G., Moffat, A. F. J., & Demers, S. 1989, ApJ, 339, 926
Gratton, R., Sneden, C., & Carretta, E. 2004, ARA&A, 42, 385
Gratton, R. G., Carretta, E., Bragaglia, A., Lucatello, S., & D'Orazi, V. 2010, A&A, 517, A81
Greenstein, G. S. 1967, Natur, 213, 871
Greenstein, J. L., & Sargent, A. I. 1974, ApJS, 28, 157
Grevesse, N., Noels, A., & Sauval, A. J. 1996, in ASP Conf. Ser. 99, Cosmic Abundances, ed. S. S. Holt & G. Sonneborn (San Francisco, CA: ASP), 117
Gualandris, A., & Portegies Zwart, S. 2007, MNRAS, 376, L29
Gvaramadze, V. V., Gualandris, A., & Portegies Zwart, S. 2008, MNRAS, 385, 929
Gvaramadze, V. V., Gualandris, A., & Portegies Zwart, S. 2009, MNRAS, 396, 570
Hattori, K., Valluri, M., Bell, E. F., & Roederer, I. U. 2018a, ApJ, 866, 121
Hattori, K., Valluri, M., & Castro, N. 2018b, ApJ, 869, 33
Hawkins, K., & Wyse, R. F. G. 2018, MNRAS, 481, 1028
Heber, U. 2009, ARA&A, 47, 211
Heber, U., Edelmann, H., Napiwotzki, R., Altmann, M., & Scholz, R.-D. 2008, A&A, 483, L21
Henden, A. A., Templeton, M., Terrell, D., et al. 2016, yCat, 2336
Hills, J. G. 1988, Natur, 331, 687
Hoogerwerf, R., de Bruijne, J. H. J., & de Zeeuw, P. T. 2001, A&A, 365, 49
Hopman, C., Portegies Zwart, S. F., & Alexander, T. 2004, ApJL, 604, L101
Huang, Y., Liu, X.-W., Zhang, H.-W., et al. 2017, ApJL, 847, L9
Hunter, J. D. 2007, CSE, 9, 90
Hut, P., & Bahcall, J. N. 1983, ApJ, 268, 319
Irrgang, A., Kreuzer, S., & Heber, U. 2018, A&A, 620, 48
Irrgang, A., Przybilla, N., Heber, U., Nieva, M. F., & Schuh, S. 2010, ApJ, 711, 138
Ishii, M., Ueno, M., & Kato, M. 1999, PASJ, 51, 417
Jones, E., Oliphant, T., Peterson, P., et al. 2001, SciPy: Open source scientific tools for Python, http://www.scipy.org/
Kato, M. 1985, PASJ, 37, 311
Kelson, D. D. 2003, PASP, 115, 688
Kelson, D. D., Illingworth, G. D., van Dokkum, P. G., & Franx, M. 2000, ApJ, 531, 159
Kerr, F. J., & Lynden-Bell, D. 1986, MNRAS, 221, 1023
Krivonos, R. A., Tsygankov, S. S., Mereminskiy, I. A., et al. 2017, MNRAS, 470, 512
Lada, C. J., & Lada, E. A. 2003, ARA&A, 41, 57
Lee, Y.-W., Demarque, P., & Zinn, R. 1994, ApJ, 423, 248
Lefever, K., Puls, J., Morel, T., et al. 2010, A&A, 515, A74
Leonard, P. J. T. 1989, AJ, 98, 217
Leonard, P. J. T. 1991, AJ, 101, 562
Li, Y.-B., Luo, A.-L., Zhao, G., et al. 2018, AJ, 156, 87
Lindegren, L. 2018, Re-normalising the astrometric chi-square in Gaia DR2, GAIA-C3-TN-LU-LL-124, http://www.rssd.esa.int/doc_fetch.php?id=3757412
Luck, R. E., & Lambert, D. L. 2011, AJ, 142, 136
Maíz Apellániz, J., Pantaleoni González, M., Barbá, R. H., et al. 2018, A&A, 616, A149
Marchetti, T., Rossi, E. M., & Brown, A. G. A. 2018, MNRAS, tmp, 2466
Martin, J. C. 2006, AJ, 131, 3047

[11] The value of u_0 is obtained from the interpolation of the look-up table available at https://www.cosmos.esa.int/web/gaia/dr2-known-issues.

McEvoy, C. M., Dufton, P. L., Smoker, J. V., et al. 2017, ApJ, 842, 32
Mdzinarishvili, T. G., & Chargeishvili, K. B. 2005, A&A, 431, L1
Messineo, M., Zhu, Q., Menten, K. M., et al. 2016, ApJL, 822, L5
Michaud, G., Alecian, G., & Richer, J. 2015, Atomic Diffusion in Stars (Cham: Springer)
Michaud, G., Vauclair, G., & Vauclair, S. 1983, ApJ, 267, 256
Miller, M. C., & Hamilton, D. P. 2002, MNRAS, 330, 232
Moehler, S., Landsman, W. B., Sweigart, A. V., & Grundahl, F. 2003, A&A, 405, 135
Moni Bidin, C., Moehler, S., Piotto, G., Momany, Y., & Recio-Blanco, A. 2007, A&A, 474, 505
Moni Bidin, C., Villanova, S., Piotto, G., Moehler, S., & D'Antona, F. 2011, ApJL, 738, L10
Nieva, M.-F., & Przybilla, N. 2012, A&A, 539, A143
Oh, K., Koss, M., Markwardt, C. B., et al. 2018, ApJS, 235, 4
Oka, T., Tsujimoto, S., Iwata, Y., Nomura, M., & Takekawa, S. 2017, NatAs, 1, 709
Origlia, L., Oliva, E., Sanna, N., et al. 2016, A&A, 585, A14
Perets, H. B., & Šubr, L. 2012, ApJ, 751, 133
Portegies Zwart, S. F. 2000, ApJ, 544, 437
Portegies Zwart, S. F., Baumgardt, H., Hut, P., Makino, J., & McMillan, S. L. W. 2004, Natur, 428, 724
Portegies Zwart, S. F., Makino, J., McMillan, S. L. W., & Hut, P. 1999, A&A, 348, 117
Portegies Zwart, S. F., McMillan, S. L. W., & Gieles, M. 2010, ARA&A, 48, 431
Posti, L., & Helmi, A. 2019, A&A, 621, 56
Poveda, A., Ruiz, J., & Allen, C. 1967, BOTT, 4, 86
Przybilla, N., Nieva, M. F., Heber, U., et al. 2008, A&A, 480, L37
Puls, J., Urbaneja, M. A., Venero, R., et al. 2005, A&A, 435, 669
Rivero González, J. G., Puls, J., Massey, P., & Najarro, F. 2012, A&A, 543, A95
Salpeter, E. E. 1955, ApJ, 121, 161
Sandage, A., & Wallerstein, G. 1960, ApJ, 131, 598
Santolaya-Rey, A. E., Puls, J., & Herrero, A. 1997, A&A, 323, 488
Schneider, F. R. N., Podsiadlowski, P., Langer, N., Castro, N., & Fossati, L. 2016, MNRAS, 457, 2355
Schönrich, R., Binney, J., & Dehnen, W. 2010, MNRAS, 403, 1829
Silva, M. D. V., & Napiwotzki, R. 2011, MNRAS, 411, 2596
Simón-Díaz, S., Godart, M., Castro, N., et al. 2017, A&A, 597, A22
Simón-Díaz, S., & Herrero, A. 2007, A&A, 468, 1063
Simón-Díaz, S., & Herrero, A. 2014, A&A, 562, A135
Tauris, T. M. 2015, MNRAS, 448, L6
Tauris, T. M., & Takens, R. J. 1998, A&A, 330, 1047
Tetzlaff, N., Neuhäuser, R., & Hohle, M. M. 2011, MNRAS, 410, 190
Vallée, J. P. 2008, AJ, 135, 1301
van der Walt, S., Colbert, S. C., & Varoquaux, G. 2011, CSE, 13, 22
Vasiliev, E. 2019, MNRAS, 482, 1525
Vink, J. S. 2015, in Very Massive Stars in the Local Universe, Vol. 412, ed. J. S. Vink (Cham: Springer), 77
Watkins, L. L., van der Marel, R. P., Sohn, S. T., & Evans, N. W. 2019, ApJ, in press (arXiv:1804.11348)
Xue, X. X., Rix, H. W., Zhao, G., et al. 2008, ApJ, 684, 1143
Yoshii, Y. 2013, in Star Counts and Nature of the Galactic Thick Disk, ed. T. D. Oswalt & G. Gilmore (Dordrecht: Springer), 393
Yu, Q., & Tremaine, S. 2003, ApJ, 599, 1129
Yungelson, L. R., van den Heuvel, E. P. J., Vink, J. S., Portegies Zwart, S. F., & de Koter, A. 2008, A&A, 477, 223
Zheng, Z., Carlin, J. L., Beers, T. C., et al. 2014, ApJL, 785, L23
Zwicky, F. 1957, Morphological Astronomy (Berlin: Springer)